The Astrophysical Journal Letters, 984:L9 (36pp), 2025 May 1 https://doi.org/10.3847/2041-8213/adc438

exoALMA. IV. Substructures, Asymmetries, and the Faint Outer Disk in Continuum Emission

Pietro Curone[1,2], Stefano Facchini[1], Sean M. Andrews[3], Leonardo Testi[4], Myriam Benisty[5,6], Ian Czekala[7], Jane Huang[8], John D. Ilee[9], Andrea Isella[10,11], Giuseppe Lodato[1], Ryan A. Loomis[12], Jochen Stadler[5], Andrew J. Winter[5,6], Jaehan Bae[13], Marcelo Barraza-Alfaro[14], Gianni Cataldi[15], Nicolás Cuello[16], Daniele Fasano[5], Mario Flock[6], Misato Fukagawa[15], Maria Galloway-Sprietsma[13], Himanshi Garg[17], Cassandra Hall[18,19,20], Andrés F. Izquierdo[13,21,22,29], Kazuhiro Kanagawa[23], Geoffroy Lesur[16], Cristiano Longarini[1,24], Francois Menard[16], Ryuta Orihara[23], Christophe Pinte[16,17], Daniel J. Price[17], Giovanni Rosotti[1], Richard Teague[14], Gaylor Wafflard-Fernandez[16], David J. Wilner[3], Lisa Wölfer[14], Hsi-Wei Yen[25], Tomohiro C. Yoshida[15,26], and Brianna Zawadzki[27,28]

[1] Dipartimento di Fisica, Università degli Studi di Milano, Via Celoria 16, 20133 Milano, Italy; pcurone@das.uchile.cl
[2] Departamento de Astronomía, Universidad de Chile, Camino El Observatorio 1515, Las Condes, Santiago, Chile
[3] Center for Astrophysics—Harvard & Smithsonian, Cambridge, MA 02138, USA
[4] Dipartimento di Fisica e Astronomia, Università di Bologna, I-40190 Bologna, Italy
[5] Université Côte d'Azur, Observatoire de la Côte d'Azur, CNRS, Laboratoire Lagrange, France
[6] Max-Planck Institute for Astronomy (MPIA), Königstuhl 17, 69117 Heidelberg, Germany
[7] School of Physics & Astronomy, University of St. Andrews, North Haugh, St. Andrews KY16 9SS, UK
[8] Department of Astronomy, Columbia University, 538 W. 120th St., Pupin Hall, New York, NY 10027, USA
[9] School of Physics and Astronomy, University of Leeds, Leeds, LS2 9JT, UK
[10] Department of Physics and Astronomy, Rice University, 6100 Main St., Houston, TX 77005, USA
[11] Rice Space Institute, Rice University, 6100 Main St., Houston, TX 77005, USA
[12] National Radio Astronomy Observatory, 520 Edgemont Rd., Charlottesville, VA 22903, USA
[13] Department of Astronomy, University of Florida, Gainesville, FL 32611, USA
[14] Department of Earth, Atmospheric, and Planetary Sciences, Massachusetts Institute of Technology, Cambridge, MA 02139, USA
[15] National Astronomical Observatory of Japan, 2-21-1 Osawa, Mitaka, Tokyo 181-8588, Japan
[16] Univ. Grenoble Alpes, CNRS, IPAG, 38000 Grenoble, France
[17] School of Physics and Astronomy, Monash University, VIC 3800, Australia
[18] Department of Physics and Astronomy, The University of Georgia, Athens, GA 30602, USA
[19] Center for Simulational Physics, The University of Georgia, Athens, GA 30602, USA
[20] Institute for Artificial Intelligence, The University of Georgia, Athens, GA 30602, USA
[21] Leiden Observatory, Leiden University, P.O. Box 9513, NL-2300 RA Leiden, The Netherlands
[22] European Southern Observatory, Karl-Schwarzschild-Str. 2, D-85748 Garching bei München, Germany
[23] College of Science, Ibaraki University, 2-1-1 Bunkyo, Mito, Ibaraki 310-8512, Japan
[24] Institute of Astronomy, University of Cambridge, Madingley Rd., CB30HA, Cambridge, UK
[25] Academia Sinica Institute of Astronomy & Astrophysics, 11F of Astronomy-Mathematics Building, AS/NTU, No. 1, Sec. 4, Roosevelt Rd., Taipei 106216, Taiwan
[26] Department of Astronomical Science, The Graduate University for Advanced Studies, SOKENDAI, 2-21-1 Osawa, Mitaka, Tokyo 181-8588, Japan
[27] Department of Astronomy, Van Vleck Observatory, Wesleyan University, 96 Foss Hill Dr., Middletown, CT 06459, USA
[28] Department of Astronomy & Astrophysics, 525 Davey Laboratory, The Pennsylvania State University, University Park, PA 16802, USA
Received 2024 November 29; revised 2025 March 6; accepted 2025 March 13; published 2025 April 28

Abstract

The exoALMA Large Program targeted a sample of 15 disks to study gas dynamics within these systems, and these observations simultaneously produced continuum data at 0.9 mm (331.6 GHz) with exceptional surface brightness sensitivity at high angular resolution. To provide a robust characterization of the observed substructures, we performed a visibility space analysis of the continuum emission from the exoALMA data, characterizing axisymmetric substructures and nonaxisymmetric residuals obtained by subtracting an axisymmetric model from the observed data. We defined a nonaxisymmetry index and found that the most asymmetric disks predominantly show an inner cavity and consistently present higher values of mass accretion rate and near-infrared excess. This suggests a connection between outer disk dust substructures and inner disk properties. The depth of the data allowed us to describe the azimuthally averaged continuum emission in the outer disk, revealing that larger disks (both in dust and gas) in our sample tend to be gradually tapered compared to the sharper outer edge of more compact sources. Additionally, the data quality revealed peculiar features in various sources, such as shadows, inner disk offsets, tentative external substructures, and a possible dust cavity wall.

Unified Astronomy Thesaurus concepts: Protoplanetary disks (1300); Dust continuum emission (412); Planet formation (1241); Radio interferometry (1346)

[29] NASA Hubble Fellowship Program Sagan Fellow.

1. Introduction

Over the last decade, the capabilities of the Atacama Large Millimeter/submillimeter Array (ALMA) allowed us to reveal and extensively explore substructures in protoplanetary disks. This effort began with the dust continuum observation of HL

Tau by ALMA Partnership et al. (2015) and has continued with numerous other high-resolution observations (see, e.g., S. M. Andrews 2020 for a review). Substructures in disks have also been detected using other tracers and wavelengths, such as in the gas line emission (e.g., C. J. Law et al. 2021) and the near-infrared (NIR) scattered light (review by M. Benisty et al. 2023). These substructures include rings and gaps (S. M. Andrews et al. 2016, 2018; F. Long et al. 2018; S. Pérez et al. 2019), cavities (S. Facchini et al. 2020; L. Francis & N. van der Marel 2020; A. Sierra et al. 2024), crescents (S. Casassus et al. 2013; N. van der Marel et al. 2013; L. M. Pérez et al. 2014), and spirals (M. Benisty et al. 2015; L. M. Pérez et al. 2016; J. Speedie et al. 2024).

Different physical mechanisms have been proposed to explain the formation of such substructures. They encompass a range of hydrodynamic and magnetohydrodynamic processes (e.g., Rossby wave instability, vertical shear instability, gravitational instability, zonal flows, dead zones), photoevaporative and magnetic winds, dust accumulation, and growth at ice lines along with dust concentration driven by streaming instability, as well as tidal interactions with a stellar companion and stellar flyby events (N. T. Kurtovic et al. 2018; J. Bae et al. 2023; N. Cuello et al. 2023; G. Lesur et al. 2023; I. Pascucci et al. 2023). Among these mechanisms, the observed substructures are often interpreted as resulting from interactions between the disk and one or more planets (e.g., B. A. Ayliffe et al. 2012; G. Dipierro et al. 2015; J. Bae et al. 2018; G. Lodato et al. 2019; A. Ruzza et al. 2024).

Among the different tracers used to study disk substructures, dust continuum emission at submillimeter wavelengths holds particular importance. Dust particles in disks constitute the fundamental building blocks of planets, and their thermal emission allows us to trace the distribution and properties of millimeter-sized grains concentrated in the disk midplane, where planet formation is thought to occur (J. Drażkowska et al. 2023). By studying dust continuum emission, we gain insights into the processes that shape dust distribution, growth, concentration, and evolution, all of which are essential for understanding the early stages of planet formation (L. Testi et al. 2014).

However, what governs the morphology of dust continuum emission in protoplanetary disks remains an open question. In this Letter, we aim to bring new insights to this question by analyzing the homogeneous, deep observations at high angular resolution of dust continuum emission from the exoALMA Large Program[30] (2021.1.01123.L; R. Teague et al. 2024). The continuum emission features observed in the exoALMA sample are then connected to properties derived from gas emission observations and model predictions in other Letters of this series (M. Galloway-Sprietsma et al. 2025; C. H. Gardner et al. 2025; C. Longarini et al. 2025; J. Stadler et al. 2025; L. Wölfer et al. 2025; C. T. Yoshida et al. 2025). Additionally, we introduce two new metrics: one to quantify the level of nonaxisymmetry in disks, used to explore connections between observed dust substructures and inner disk properties, and another to investigate the falloff of the outer disk emission.

Section 2 presents the exoALMA data. Section 3 describes the pipeline adopted to characterize the observed substructures in the visibility space. Section 4 presents the results of the analysis, including axisymmetric substructures and nonaxisymmetric residuals obtained by subtracting an axisymmetric model from the data. Section 5 discusses the results by examining the observed substructures in the context of what is already known for each disk. We also discuss nonaxisymmetries, the faint outer disk, and hints of the presence of companions in the disks in our sample, comparing our findings with previous studies and with the velocity kink results presented by C. Pinte et al. (2025). Section 6 summarizes the main results.

[30] https://www.exoalma.com

2. Data

exoALMA targeted 15 protoplanetary disks with deep observations at high angular and spectral resolution. The primary objective was to study the physical and dynamical structure of the gas in these disks and to reveal perturbations that may be produced by embedded planets (R. Teague et al. 2024). For this aim, as detailed in R. Teague et al. (2024), the selection criteria focused on sources that were extended in gas (at least 1″) and had favorable inclinations (between $\sim 5^{\circ}$ and 60°) and whose gas emission was free from absorption or contamination by large-scale emission. Preference was given to brighter sources in ^{12}CO, with a distribution in R.A. to facilitate scheduling observations. This resulted in an intentionally biased sample toward bright and extended disks from different star-forming regions, most of which have already been observed in continuum by ALMA at high angular resolution, revealing a variety of dust substructures indicative of planet–disk interactions.

The exoALMA observations also produced extremely deep dust continuum data at high angular resolution. Observations were carried out in ALMA Band 7, combining configurations C-6 and C-3 (and the Atacama Compact Array, ACA, for the most extended sources), having one spectral window with a bandwidth of 1875 MHz centered at 331.57 GHz (0.904 mm) dedicated to the continuum emission. This resulted in continuum images with an angular resolution of $\sim$0.″09, a maximum recoverable scale of 4.″7 (19.″3 for sources with ACA observations), and a sensitivity of $\sim 40\,\mu$Jy beam^{-1}. The exoALMA observations provide deep surface brightness sensitivity at high angular resolution, achieving a noise level of $\sim$0.05 K. For comparison, the DSHARP program (S. M. Andrews et al. 2018) reached a noise level of 0.25 K at a wavelength of 1.3 mm and a resolution of $\sim$0.″035 (both noise levels calculated using the Rayleigh–Jeans approximation).

Pipeline calibration and self-calibration have been applied to all sources. A dedicated description of the calibration and imaging pipeline is presented in R. Loomis et al. (2025). For the analyses in this Letter, we considered only the spectral window dedicated to the continuum to maintain consistency in frequency coverage, as including the additional continuum data in spectral windows dedicated to line emission would have provided only a marginal 3% increase in sensitivity. The visibilities in the continuum spectral windows were spectrally averaged down to one channel for each execution block and averaged in time down to 30 s bins to reduce file size and improve processing efficiency. We verified that this averaging did not affect the continuum analysis by comparing images produced with and without the averaging; the resulting images showed no significant differences (R. Loomis et al. 2025). All the manipulations of the visibilities were conducted with the software CASA, version 6.2 (CASA Team et al. 2022).

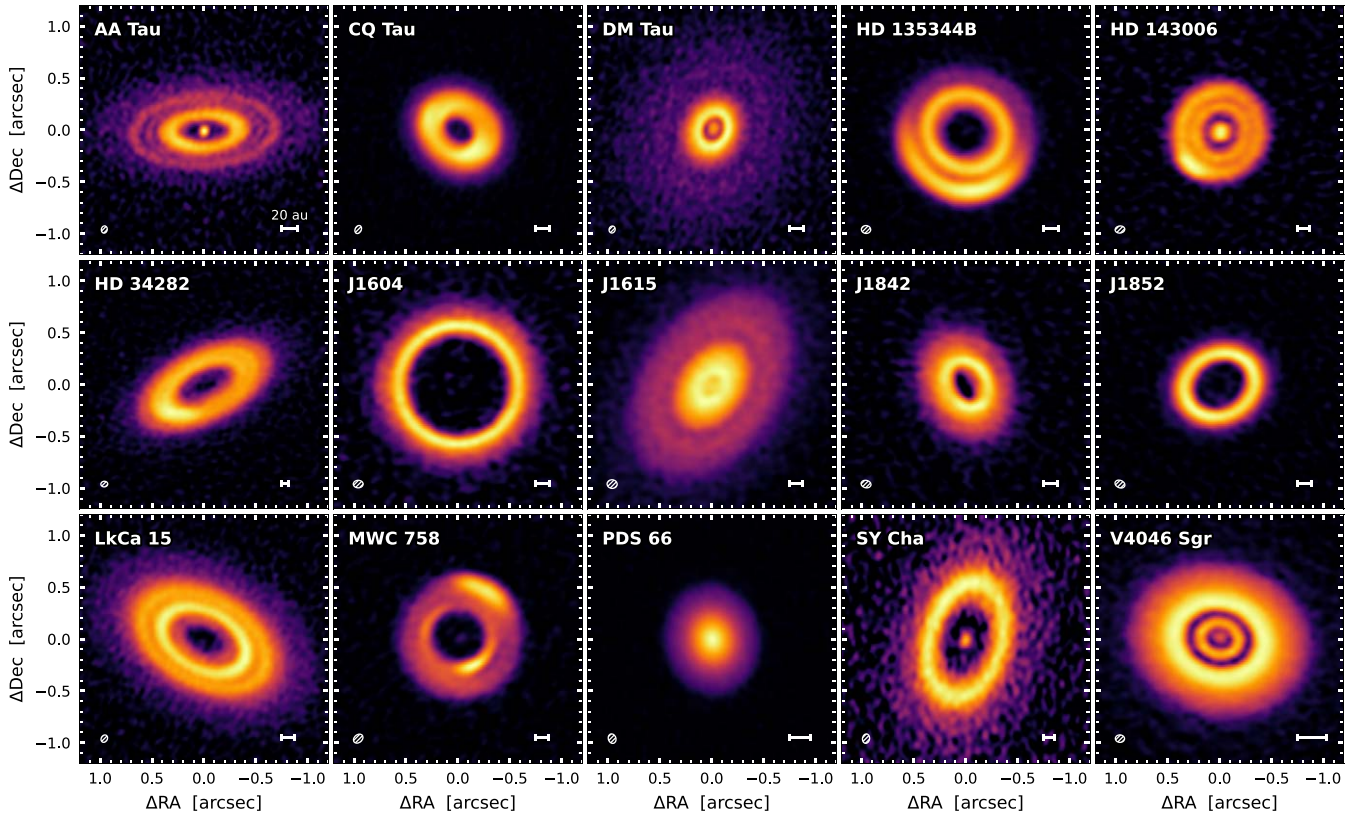

Figure 1. Gallery of fiducial continuum images at 0.9 mm (331.6 GHz) of the exoALMA sample, obtained with the CLEAN algorithm and robust of −0.5. The source order is alphabetical. All images are shown on the same angular scales. The FWHM of the synthesized beams and the 20 au scale bars are indicated in the lower left and right corners of each plot, respectively. The color scale ranges from null to peak intensity for each disk. An asinh stretch is applied to the color scale to visually enhance the fainter emission. A linear stretch version is presented in Figure A1.

Table 1
Continuum Image Properties

Source	θ_b (mas, au)	PA_b (deg)	rms Noise (μJy beam^{-1}, K)	Peak I_ν, T_b (mJy beam^{-1}, K)	F_ν (mJy)	d (pc)	M_d ($M_\oplus$, M_{Jup})
(1)	(2)	(3)	(4)	(5)	(6)	(7)	(8)
AA Tau	70 × 57, 9 × 8	168	45, 3.3	2.71, 14.0	189.4 ± 0.3	135[a]	37, 0.12
CQ Tau	82 × 59, 12 × 9	153	40, 3.1	8.10, 25.8	431.9 ± 0.3	149[a]	103, 0.33
DM Tau	68 × 58, 10 × 8	162	39, 3.2	2.98, 14.8	226.5 ± 0.6	144	50, 0.16
HD 135344B	90 × 76, 12 × 10	85	43, 2.9	6.44, 17.2	424.7 ± 0.2	135	83, 0.26
HD 143006	94 × 68, 16 × 11	97	45, 3.0	3.44, 12.3	155.5 ± 0.2	167	47, 0.15
HD 34282	67 × 54, 21 × 17	95	40, 3.3	3.80, 18.5	343.4 ± 0.3	309	351, 1.10
J1604	95 × 73, 14 × 11	91	43, 2.9	2.72, 10.4	198.4 ± 0.3	145	44, 0.14
J1615	97 × 83, 15 × 13	85	38, 2.8	5.83, 14.5	386.0 ± 0.7	156	100, 0.32
J1842	97 × 72, 15 × 11	78	43, 2.9	3.55, 12.0	141.5 ± 0.2	151	35, 0.11
J1852	99 × 71, 15 × 10	67	37, 2.8	4.52, 13.6	150.9 ± 0.1	147	35, 0.11
LkCa 15	75 × 59, 12 × 9	150	34, 3.1	2.75, 13.3	407.1 ± 0.4	156	108, 0.34
MWC 758	101 × 75, 16 × 12	130	56, 3.0	6.85, 16.7	214.5 ± 0.2	156	56, 0.18
PDS 66	93 × 73, 9 × 7	19	47, 3.0	16.28, 33.9	336.1 ± 0.2	98	35, 0.11
SY Cha	91 × 68, 16 × 12	171	56, 3.1	1.54, 8.3	158.4 ± 0.5	182	55, 0.17
V4046 Sgr	89 × 72, 6 × 5	88	37, 2.9	5.20, 15.7	668.4 ± 1.0	72	37, 0.12

Notes. All properties were obtained from fiducial CLEAN images with robust −0.5. The mean frequency is 331.6 GHz for each image. Column (1): target name. Column (2): synthesized beam FWHM major and minor axes. Column (3): synthesized beam PA. Column (4): image rms noise. Column (5): image peak intensity. Note that the noise and peak brightness temperature were computed using the full Planck law. Column (6): integrated flux density with statistical uncertainty, excluding the 10% absolute flux calibration. Column (7): source distance as measured by Gaia DR3 (Gaia Collaboration et al. 2023). Column (8): estimated dust mass.
[a] As reported in R. Teague et al. (2024), the renormalized unit weight error (RUWE) values from Gaia (Gaia Collaboration et al. 2023) for these sources are high, indicating that their distances should be interpreted with caution.

We present a gallery of the fiducial continuum images of the exoALMA disks in Figure 1 with an asinh stretch on the color scale (meaning the asinh function has been applied to the observed intensity) and in Figure A1 with a linear stretch. Table 1 reports the properties of the observed continuum images for each target. We calculated the rms noise in an

annulus between 3″ and 4″ centered on the disk, where no emission from the target was present. Integrated flux density was measured within a mask defined as an ellipse with the same center, position angle (PA), and aspect ratio as the target. The semimajor axis of this ellipse is 1.5 times the outer extent of the observed emission ($R_{\rm out}$), determined by the intersection of the contour reaching twice the rms noise level in the image with the disk major axis. The associated uncertainty reflects only the statistical error and does not include the 10% absolute flux error (2σ) in ALMA Band 7 observations.[31] To estimate the statistical error, we followed a procedure similar to that of L. Rampinelli et al. (2024). We computed the uncertainty as the standard deviation of the integrated flux density measured in 24 nonoverlapping elliptical masks identical to the one used for the disk's flux measurement placed within the field of view (FOV) outside the disk's emitting area. Since the continuum emission is always well within the primary beam, we used images without primary beam correction to yield uniform noise.

We derived an estimate of the total dust mass in each disk using the integrated flux density and the relation from R. H. Hildebrand (1983), which is based on the assumption of optically thin dust emission,

$$M_{\rm d} = \frac{F_\nu d^2}{B_\nu(T) k_\nu}, \tag{1}$$

where d is the distance, $B_\nu(T)$ is the blackbody surface brightness at a given temperature, and k_ν is the dust opacity. We assumed a temperature of 20 K (as in, e.g., M. Ansdell et al. 2016) and an opacity $k_\nu = 3.5\,{\rm cm^2\ g^{-1}} \times 870\,\mu{\rm m}/\lambda$ (S. V. W. Beckwith et al. 1990). C. Longarini et al. (2025) provide a comparison between the masses derived from the continuum and the ones computed from the gas rotation curves. They obtain gas-to-dust mass ratios above the usual value of 100, with an average of ∼400. These high values indicate that the dust masses we compute are underestimated due to the assumption of optically thin emission when using Equation (1).

3. Methods for the Continuum Analysis

The first aim of our continuum data analysis is to perform a morphological characterization of the observed substructures in each disk. To do so, we rely on a two-step visibility-fitting pipeline.[32]

First, we use the code `galario` (M. Tazzari et al. 2018) to recover the disk's geometric parameters: inclination (i), PA, and the offsets in R.A. and decl. between the disk center and the phase center (ΔR.A. and Δdecl.; Section 3.1). `galario` uses a parametric intensity model and a Markov Chain Monte Carlo (MCMC) approach, which ensures accurate estimation of the disk geometry, as demonstrated in several previous studies (e.g., D. Fedele et al. 2018; F. Long et al. 2018; S. Facchini et al. 2020).

We then use these geometric parameters as input in the second step, where, to obtain a model of the intensity radial profile, we employ `frankenstein` (hereafter `frank`; J. Jennings et al. 2020). Unlike `galario`, `frank` uses a nonparametric approach, offering more flexibility in fitting the observed visibilities without requiring a predefined intensity model. This nonparametric method allows us to reconstruct the intensity radial profile with subbeam resolution, providing a more detailed representation of the disk structure (Section 3.2).

3.1. `Galario` Fit

The code `galario` assumes a 1D or 2D model representing the emission in the image plane and performs a Fourier transform to derive the synthetic visibilities at the same uv-points as the observation (M. Tazzari et al. 2018). The best-fit model is determined by minimizing the χ^2 through an MCMC approach, utilizing the `emcee` package for parameter sampling (D. Foreman-Mackey et al. 2013). In employing this methodology, our primary focus was not an exhaustive characterization of the substructures, a task reserved for the application of `frank`. Instead, our objective was to derive robust estimates of the geometrical parameters of each disk, specifically inclination, PA, and offsets in R.A. and decl. between the disk center and the phase center. This is reflected by our choices of the parametric models, selected so that they could globally represent the disk observed morphology.

Of the 15 sources, 10 were characterized using 1D axisymmetric intensity profiles. Each profile includes one or more Gaussian rings,

$$I(R) = f_0 \exp\left[-\frac{(R - R_0)^2}{2\sigma^2}\right], \tag{2}$$

where R is the radial coordinate, f_0 is a normalization term, R_0 denotes the radial location of the Gaussian peak, and σ is the standard deviation. For sources displaying inner emission, we added either a central Gaussian,

$$I(R) = f_0 \exp\left[-\frac{R^2}{2\sigma^2}\right], \tag{3}$$

or, in the case of unresolved emission, a central point source,

$$I(R) = f_0\ \delta(R), \tag{4}$$

where $\delta(R)$ is the Dirac delta function.

For the five disks showing strong asymmetries (CQ Tau, HD 135344B, HD 143006, HD 34282, and MWC 758), we employed 2D models. These models combined axisymmetric rings with one or more arcs (as done by, e.g., P. Cazzoletti et al. 2018 and L. M. Pérez et al. 2018), defined as Gaussian rings with azimuthal tapering,

$$I(R, \phi) = f_0 \exp\left[-\frac{(R - R_0)^2}{2\sigma^2}\right] \times \exp\left[-\frac{(\phi - \phi_0)^2}{2\sigma_\phi^2}\right], \tag{5}$$

where ϕ is the azimuthal coordinate, ϕ_0 is the azimuthal center of the arc, and σ_ϕ is its azimuthal extent.

Uniform priors were applied, and the intensity normalization factor f_0 was logarithmically sampled. For each 1D calculation, we used ∼100 walkers that converged after $\sim 10^4$ steps, while the 2D runs required a higher number of steps to converge, between $\sim 3 \times 10^4$ and $\sim 10^5$. The estimates of the geometrical parameters for each disk are reported in Table 2, while the chosen `galario` models along with the best-fit value for each

[31] See Section 10.2.6 in the ALMA Technical Handbook: https://almascience.nrao.edu/proposing/technical-handbook/.

[32] The pipeline is accessible at https://github.com/pcurone/exoALMA_continuum_pipeline.

Table 2
Dust Disk Geometries

Source	i	PA	ΔR.A.	ΔDecl.	R_{68}	R_{90}	R_{95}
	(deg)	(deg)	(mas)	(mas)	(au, mas)	(au, mas)	(au, mas)
(1)	(2)	(3)	(4)	(5)	(6)	(7)	(8)
AA Tau	$58.54^{+0.02}_{-0.02}$	$93.77^{+0.02}_{-0.03}$	$-5.46^{+0.11}_{-0.11}$	$4.83^{+0.07}_{-0.08}$	$92.2^{+1.2}_{-0.6}$, 685^{+9}_{-5}	$139.4^{+1.2}_{-1.2}$, 1035^{+9}_{-9}	$158.6^{+2.2}_{-1.2}$, 1177^{+16}_{-9}
CQ Tau	$35.24^{+0.02}_{-0.02}$	$53.87^{+0.02}_{-0.02}$	$-8.71^{+0.05}_{-0.05}$	$0.99^{+0.04}_{-0.04}$	$55.8^{+0.6}_{-0.1}$, 373^{+4}_{-1}	$73.1^{+0.6}_{-0.6}$, 489^{+4}_{-4}	$85.4^{+0.7}_{-0.1}$, 572^{+5}_{-1}
DM Tau	$35.97^{+0.05}_{-0.05}$	$155.60^{+0.08}_{-0.07}$	$-5.51^{+0.07}_{-0.07}$	$-6.59^{+0.09}_{-0.09}$	$118.6^{+0.8}_{-0.8}$, 824^{+6}_{-6}	$201.9^{+1.6}_{-0.8}$, 1402^{+11}_{-6}	$244.8^{+1.6}_{-1.6}$, 1700^{+11}_{-11}
HD 135344B	$20.73^{+0.02}_{-0.02}$	$28.92^{+0.09}_{-0.06}$	$0.80^{+0.05}_{-0.05}$	$-3.21^{+0.05}_{-0.05}$	$78.7^{+1.2}_{-1.2}$, 583^{+9}_{-9}	$90.2^{+1.2}_{-1.2}$, 668^{+9}_{-9}	$94.4^{+1.2}_{-0.6}$, 700^{+9}_{-4}
HD 143006	$18.69^{+0.09}_{-0.09}$	$7.53^{+0.35}_{-0.32}$	$8.27^{+0.14}_{-0.13}$	$26.42^{+0.16}_{-0.16}$	$69.4^{+0.4}_{-0.4}$, 415^{+2}_{-2}	$79.9^{+1.1}_{-0.8}$, 478^{+7}_{-4}	$84.8^{+1.5}_{-0.8}$, 507^{+9}_{-4}
HD 34282	$59.09^{+0.01}_{-0.01}$	$117.15^{+0.01}_{-0.01}$	$13.00^{+0.07}_{-0.08}$	$15.49^{+0.06}_{-0.06}$	$179.8^{+2.8}_{-1.4}$, 583^{+9}_{-4}	$239.4^{+2.8}_{-2.8}$, 776^{+9}_{-9}	$289.3^{+3.2}_{-2.8}$, 938^{+10}_{-9}
J1604	$8.72^{+0.09}_{-0.07}$	$123.24^{+0.07}_{-0.15}$	$-74.82^{+0.07}_{-0.07}$	$-16.67^{+0.06}_{-0.06}$	$94.0^{+0.5}_{-0.1}$, 650^{+4}_{-1}	$112.4^{+0.5}_{-0.1}$, 778^{+4}_{-1}	$122.2^{+0.1}_{-0.5}$, 845^{+1}_{-4}
J1615	$47.10^{+0.01}_{-0.01}$	$146.14^{+0.02}_{-0.02}$	$-44.32^{+0.05}_{-0.04}$	$-5.88^{+0.04}_{-0.05}$	$116.1^{+1.0}_{-0.1}$, 746^{+7}_{-1}	$169.6^{+2.1}_{-1.0}$, 1090^{+13}_{-7}	$204.2^{+2.1}_{-1.0}$, 1312^{+13}_{-7}
J1842	$39.22^{+0.03}_{-0.04}$	$26.35^{+0.06}_{-0.06}$	$-3.16^{+0.07}_{-0.07}$	$-30.69^{+0.07}_{-0.07}$	$62.7^{+0.5}_{-0.1}$, 415^{+4}_{-1}	$85.2^{+1.1}_{-0.5}$, 564^{+7}_{-4}	$100.8^{+0.5}_{-1.1}$, 668^{+4}_{-7}
J1852	$32.50^{+0.03}_{-0.05}$	$117.61^{+0.03}_{-0.03}$	$-23.41^{+0.04}_{-0.04}$	$1.91^{+0.04}_{-0.04}$	$58.0^{+0.7}_{-0.1}$, 394^{+4}_{-1}	$69.9^{+0.7}_{-0.7}$, 475^{+4}_{-4}	$79.8^{+0.7}_{-0.7}$, 542^{+4}_{-4}
LkCa 15	$50.59^{+0.01}_{-0.02}$	$61.57^{+0.01}_{-0.01}$	$-16.84^{+0.05}_{-0.05}$	$20.83^{+0.05}_{-0.05}$	$111.0^{+1.6}_{-0.8}$, 706^{+10}_{-5}	$156.3^{+2.5}_{-1.6}$, 994^{+16}_{-10}	$181.0^{+2.5}_{-2.5}$, 1152^{+16}_{-16}
MWC 758	$7.27^{+0.23}_{-0.17}$	$76.17^{+0.13}_{-0.10}$	$25.48^{+0.13}_{-0.13}$	$18.42^{+0.12}_{-0.12}$	$79.5^{+0.4}_{-0.8}$, 510^{+3}_{-5}	$91.4^{+1.2}_{-1.2}$, 586^{+8}_{-8}	$96.3^{+1.2}_{-1.2}$, 618^{+8}_{-8}
PDS 66	$32.02^{+0.03}_{-0.03}$	$8.91^{+0.05}_{-0.05}$	$-3.59^{+0.02}_{-0.02}$	$6.68^{+0.03}_{-0.03}$	$31.7^{+0.3}_{-0.1}$, 324^{+3}_{-1}	$46.9^{+0.3}_{-0.3}$, 479^{+3}_{-3}	$51.5^{+0.5}_{-0.3}$, 526^{+5}_{-3}
SY Cha	$51.65^{+0.03}_{-0.02}$	$165.77^{+0.04}_{-0.04}$	$-12.66^{+0.12}_{-0.13}$	$28.16^{+0.18}_{-0.18}$	$132.3^{+1.6}_{-1.6}$, 732^{+9}_{-9}	$197.7^{+2.4}_{-1.6}$, 1094^{+13}_{-9}	$228.1^{+1.6}_{-1.6}$, 1262^{+9}_{-9}
V4046 Sgr	$33.36^{+0.01}_{-0.01}$	$76.02^{+0.02}_{-0.01}$	$-50.94^{+0.03}_{-0.02}$	$-45.18^{+0.02}_{-0.02}$	$46.5^{+0.1}_{-0.4}$, 650^{+1}_{-6}	$60.9^{+0.4}_{-0.4}$, 852^{+6}_{-6}	$71.8^{+0.8}_{-0.4}$, 1004^{+11}_{-6}

Note. Column (1): target name. Column (2): disk inclination. Column (3): disk PA. Columns (4) and (5): offsets in R.A. and decl. between the disk center and the phase center. Geometrical parameters in columns (2)–(5) were obtained from `galario` fits (See Section 3.1), and the associated statistical uncertainties represent the 16th and 84th percentiles of the MCMC marginalized distribution. These uncertainties should not be considered as actual observational errors but rather as uncertainties on the fit given the assumed model. Columns (6), (7), and (8): radial extent of the continuum emission enclosing 68%, 90%, and 95% of the continuum intensity, respectively. Values were computed from `frank` model intensity profiles, and 16th and 84th percentiles are derived via bootstrapping varying the geometrical parameters (see Section 3.2).

parameter are presented in Tables B1 and B2 for 1D and 2D models, respectively. Appendix C compares the continuum geometrical parameters obtained with `galario` with the estimates from the gas data retrieved with `discminer` (A. F. Izquierdo et al. 2025), showing a generally good agreement (within 5° for i and PA and within 50 mas in ΔR.A. and Δdecl. in most sources).

3.2. `frank` Fit

For a thorough characterization of the intensity profiles as a function of disk radius, we used the code `frank`. It reconstructs the protoplanetary disk intensity radial profile by modeling it as a Fourier–Bessel series, then using a discrete Hankel transform to compute synthetic visibilities. These synthetic visibilities are subsequently fitted directly to the observed visibilities within a Bayesian framework, employing a Gaussian process for regularization (J. Jennings et al. 2020). This method is applied to visibilities that have been deprojected, shifted so that the center of the disk is at phase center, and left unbinned. The fit is nonparametric and 1D, assuming the axisymmetry of the source. Moreover, the disk emission is treated as geometrically flat and optically thick, since visibility deprojection based on inclination scales the total flux. `frank` enables the recovery of subbeam resolution features that remain undetected in both the CLEAN image and its azimuthally averaged intensity profile while exploiting the full data sensitivity (S. M. Andrews et al. 2021; J. D. Ilee et al. 2022; J. Jennings et al. 2022).

We performed the `frank` fit in logarithmic intensity space, which intrinsically guarantees the intensity to be nonnegative and largely reduces the high-frequency oscillations in the reconstructed intensity profile when compared to the fit in linear space. We verified that the choice of the five hyperparameters α, $w_{\rm smooth}$, $R_{\rm max}$, N, p_0) had minimal impact on the resulting fit, given the high sensitivity of our data. We selected, nonetheless, conservative values to minimize the chance of artifacts generated by fitting low signal-to-noise features and set $\alpha = 1.3$, and $w_{\rm smooth} = 0.01$, with α determining the signal-to-noise ratio (SNR) threshold at which the model stops fitting the data and $w_{\rm smooth}$ helping to suppress noisy oscillations. The hyperparameter $R_{\rm max}$, indicating the point beyond which `frank` assumes zero emission, was established at $1.5R_{\rm out}$ (see Section 2 for the definition of $R_{\rm out}$). The N hyperparameter, determining the radial gridding, was set to 400, and p_0, acting in the regularization of the emission power spectrum, was fixed to 10^{-35}, the standard value for logarithmic intensity space fitting. A comparison of the observed visibility profiles as a function of deprojected baseline with the `galario` and `frank` fits is presented in Figure B1.

As explained by J. Jennings et al. (2020, 2022), obtaining an accurate estimate of the uncertainty associated with the `frank` fit is not feasible. This limitation arises from the inherently ill-posed nature of reconstructing brightness from Fourier data. Specifically, there is no robust method to accurately extrapolate visibility amplitudes in a given data set beyond the longest baseline fitted by `frank`. Therefore, to obtain a reasonable uncertainty for the reconstructed intensity radial profile, we bootstrapped the `frank` fit by randomly varying the geometrical parameters, similar to what was done by A. S. Carvalho et al. (2024). We ran the `frank` fit 500 times for each disk (after testing that 500 iterations produced the same effect as 5000 iterations), randomly picking the i, PA, ΔR.A., and Δdecl. from a Gaussian distribution centered on the best-fit values from `galario`. Since the uncertainties on the geometric parameters from `galario` are considerably underestimated (as is often the case with MCMC methods), we

assumed broader ranges for the bootstrapping. The standard deviation was set to 1° for inclination and PA and one-third of the σ of the synthesized beam major axis for the R.A. and decl. offsets, resulting in a ∼10 mas centering accuracy. We then fitted the distribution of the intensity for each radial bin with a Gaussian and took 1σ as the uncertainty associated with the intensity. We also used this bootstrapping method to assign an uncertainty to the values of the dust disk extent (R_{68}, R_{90}, and R_{95}) reported in Table 2. These values were calculated for each iteration of the bootstrap, and the uncertainties were taken as the 16th and 84th percentiles.

4. Results

4.1. Axisymmetric Substructures

We employed the intensity profile from the `frank` fit to define the annular axisymmetric features, that is, rings and gaps. Figure 2 presents the intensity profiles as a function of disk radius of the deprojected and azimuthally averaged data CLEAN image compared to the `frank` model. The deprojection and azimuthal averaging of the observed CLEAN image were performed with the package `GoFish` (R. Teague 2019). The uncertainty was determined by dividing the 1σ scatter at each intensity radial bin by the square root of the number of beams within the corresponding radial annulus.

Considering the subbeam resolution `frank` model of the intensity radial profile, we aim to define annular substructures, that is, rings and gaps that appear as peaks and troughs in the intensity, respectively. Following the nomenclature of J. Huang et al. (2018), we label rings as "B" (for bright) and gaps as "D" (for dark). To ensure that these features are not simply noise or artifacts from the `frank` model, we establish four criteria to assess what can be robustly defined as a substructure and determine its radial location (R_B and R_D, respectively). First, focusing only on the best-fit `frank` model intensity radial profile (and not the bootstrapped uncertainties), rings and gaps must correspond to local maxima and minima, respectively. Second, their radial location should fall within the radius enclosing 90% of the source flux (R_{90}) to exclude low-SNR oscillations at larger radii. Third, the peak intensity of each ring must be higher than the rms noise to avoid low-SNR fluctuations within inner cavities. Finally, defining the gap depth as I_D/I_B, where I_D is the intensity of the gap minimum at R_D and I_B is the ring peak intensity at R_B (following the definition in J. Huang et al. 2018), we accept a pair of gap–ring if it meets the gap depth condition $I_D/I_B \leqslant 0.97$ to ensure sufficient contrast.

We adopted the procedure of J. Huang et al. (2018; see their Section 3.2 and Appendix B for more details) to determine the substructure width. Briefly, it involves deriving the width based on the inner and outer edges of a substructure rather than employing a Gaussian fit, a more suitable method for structures deviating from a Gaussian shape. Applying these criteria to our `frank` model intensity profiles, for a gap–ring pair, the dividing point between the outer edge of the gap and the inner edge of the ring, denoted as $R_{D,out} \equiv R_{B,in}$, is defined as the radius at which the intensity equals $I_{mean} = (I_D + I_B)/2$. The radius of the gap inner edge $R_{D,in}$ is the largest radius with $R < R_D$ and $I(R) = I_{mean}$. The radius of the ring outer edge $R_{B,out}$ is the smallest radius with $R > R_B$ and $I(R) = I_{mean}$. Consequently, the gap width is given by $R_{D,out} - R_{D,in}$, and the ring width is $R_{B,out} - R_{B,in}$. With this approach, we automatically obtain the width of the inner cavities as well. If the first substructure in a disk (counting from the center) is a ring (CQ Tau, HD 143006, J1604, J1842, J1852), the outer radius of the cavity corresponds to the $R_{B,in}$ of that first ring. Conversely, if the first substructure is a gap, occurring when there is an inner disk (AA Tau, DM Tau, HD 135344B, HD 34282, J1615, LkCa 15, MWC 758, SY Cha, V4046 Sgr), the outer radius of the cavity corresponds to the $R_{D,out}$ of that first gap.

All the substructure properties for each disk are presented in Table A1. PDS 66 is the only source where no annular substructures were detected.

4.2. Nonaxisymmetric Substructures

We extracted the nonaxisymmetric substructures by computing the residuals between the observed data and the axisymmetric `frank` fit. Initially, we sampled the `frank` model at the same *uv*-coordinates as the observed data, generating the synthetic visibilities for the fit. Then, we calculated the residual visibilities by subtracting these synthetic visibilities from the corresponding observed ones at each *uv*-location. We imaged the residual visibilities using the CASA `tclean` algorithm.

We present in Figure 3 and in Figures A2, A3, A4, A5, A6, A7, and A8 in Appendix A a gallery for each disk displaying the image of the observed data, the `frank` profile swept over 2π, the `frank` model imaged with CLEAN, the nonaxisymmetric residuals, and the polar plots of the data and the nonaxisymmetric residuals. The residuals are expressed in terms of the observed rms noise, indicating the nonaxisymmetry SNR. Both the data and the residuals are imaged with robust −0.5, which gave the best compromise between angular resolution and SNR (R. Loomis et al. 2025). The polar plots were computed by deprojecting and then mapping the intensity distribution onto a radius–azimuthal angle grid. For consistency with the other Letters in the exoALMA series, we adopted the same convention used by `discminer` for the azimuthal angle in polar plots (A. F. Izquierdo et al. 2025). Specifically, $\phi = 0°$ coincides with the PA measured on gas data, corresponding to the direction along the disk's semimajor axis on the redshifted side, with the azimuthal angle increasing counterclockwise. Note that the PA measured on gas data by `discminer` may differ from the one measured on continuum data by `galario` and employed in the `frank` model (see Appendix C).

We quantify the level of nonaxisymmetry by evaluating the `frank` residuals normalized by the flux in the CLEAN image of the `frank` model. We define the nonaxisymmetry index (NAI) as

$$\mathrm{NAI} = \frac{\sum_{i,j}|I_{\mathrm{res}\,i,j}|}{\sum_{i,j}|I_{\mathrm{mod}\,i,j}|} \quad \text{for SNR} \geqslant 5, \tag{6}$$

where $I_{\mathrm{res}\,i,j}$ and $I_{\mathrm{mod}\,i,j}$ are the intensity of pixel i, j of the CLEAN images of the `frank` residuals and the `frank` model. The sums are taken over all pixels within a mask defined by pixels having SNR $\geqslant 5$ in the CLEAN image of the data. CLEAN images of the data, `frank` residuals, and `frank` model must be computed with the same `tclean` parameters, particularly the same pixel size. This index represents a global deviation in flux between observed data and the `frank` axisymmetric model. A similar yet distinct approach has been

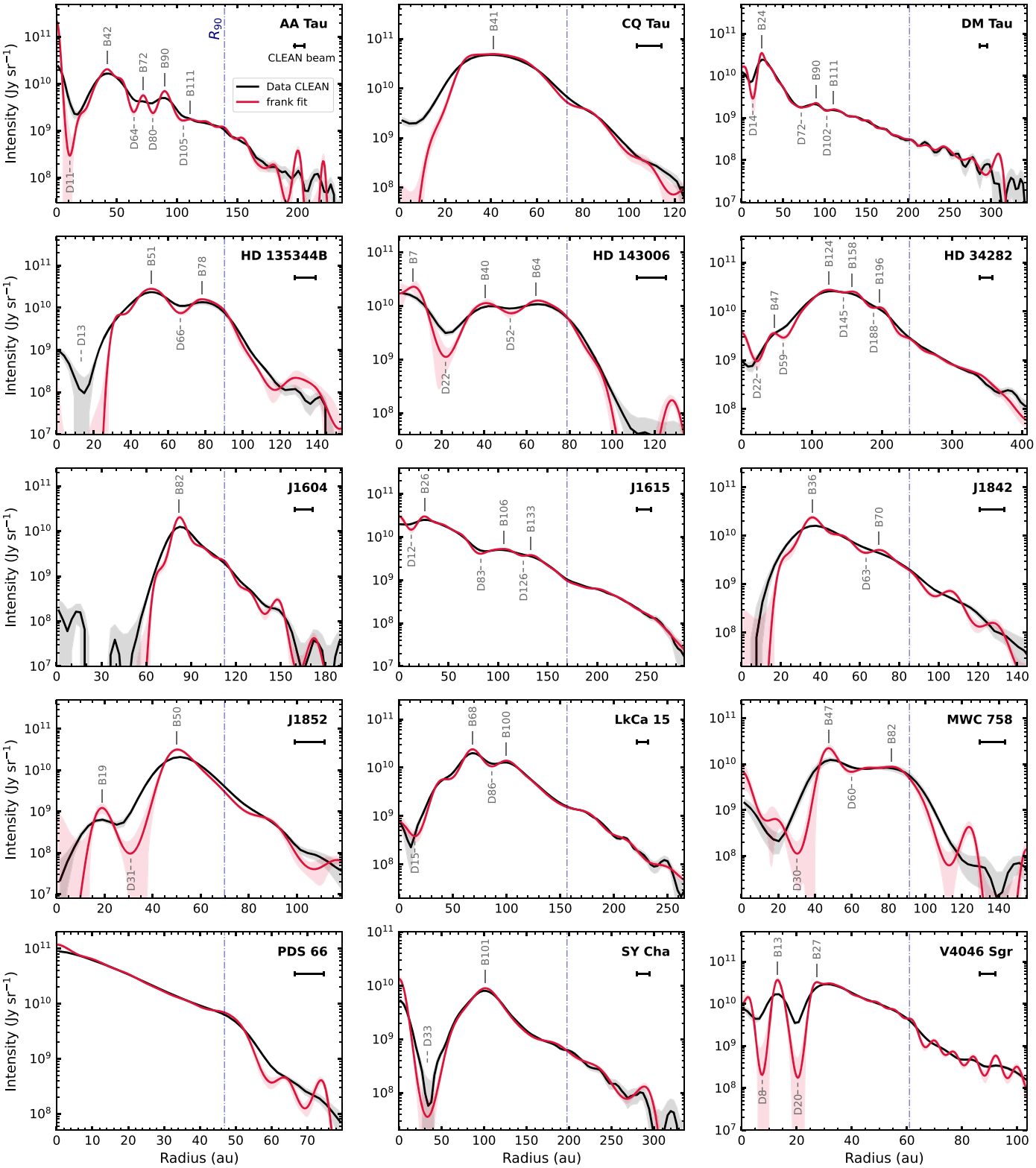

Figure 2. Gallery of radial intensity profiles on a log-linear scale of the deprojected and azimuthally averaged CLEAN data (black solid line) and the `frank` model (red solid line). Sources are arranged alphabetically. The gray shading represents CLEAN data uncertainty, calculated as the 1σ scatter per radial bin, divided by the square root of the number of beams in the associated annulus. The red shading indicates the 1σ uncertainty of the `frank` model, estimated via bootstrapping, considering small variations of the disk geometrical parameters (see Section 3.2). The black scale bar in the top right corner of each panel shows the FWHM, averaged between the major and minor axes of the CLEAN synthesized beam. Radial positions of rings and gaps are marked, with each gap labeled with a dashed line and a "D" (for dark) followed by the distance from the central star in au. Solid lines with "B" labels (for bright) denote the rings. A vertical blue dashed–dotted line indicates R_{90}, the radial location within which axisymmetric substructures are defined.

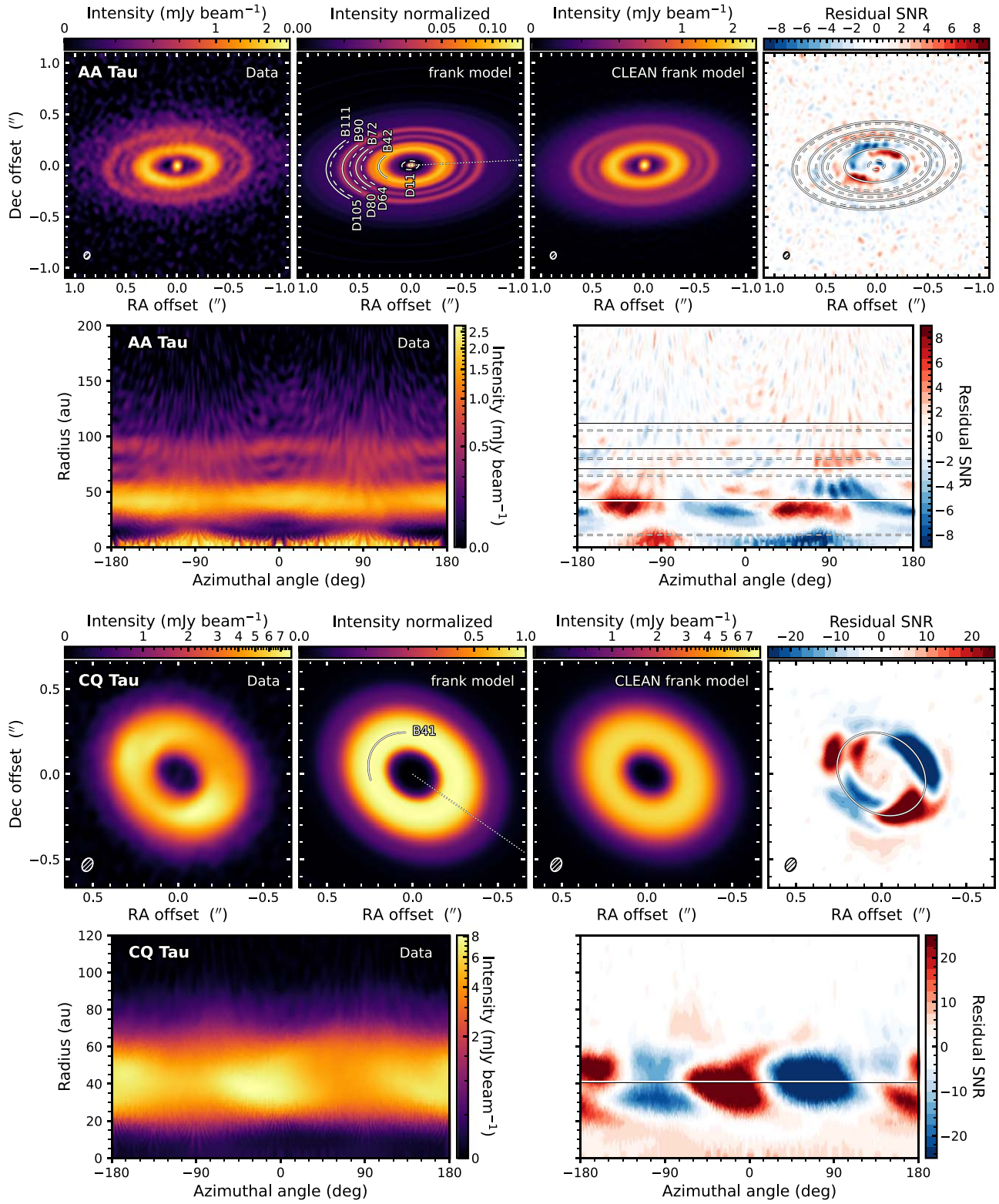

Figure 3. Comparison of the data, `frank` model, CLEAN-imaged `frank` model, residuals, and polar plots for each disk (here showing AA Tau and CQ Tau and continued in Appendix A). (Top to bottom, left to right) First panel: fiducial continuum image of the observed data obtained with robust −0.5, with the synthesized beam's FWHM shown as an ellipse in the lower left corner. The asinh function was applied to the color scale to visually enhance the fainter emission. Second panel: image of the frank model swept over 2π and reprojected, with normalized intensity and an asinh stretch. Each gap is marked by a dashed arc labeled "D" with its distance from the star in au, while solid arcs labeled "B" indicate the rings. The dotted line corresponds with the PA measured on gas data with `discminer` (A. F. Izquierdo et al. 2025) and defines the $\phi = 0$ angle of the polar plots, increasing counterclockwise (note possible PA differences with the one measured from `galario` and used in `frank`; see Appendix C). Third panel: `frank` model sampled at the same *uv*-points of the observation and imaged with CLEAN as the observed data. The color scale is the same as the data panel. Fourth panel: residuals obtained subtracting the `frank model` from the data. The residual visibilities were calculated at the same *uv*-points of the ALMA observations and imaged with CLEAN as the observed data. The color scale shows the residuals in units of the observed noise ($\sigma_{\rm rms}$). Rings and gaps are marked with solid and dashed ellipses, respectively. Fifth panel: polar plot of the data continuum image. Sixth panel: polar plot of the nonaxisymmetric residuals. The locations of rings and gaps are marked by solid and dashed horizontal lines, respectively.

applied to quantify the asymmetries in the gas emission of nearby galaxies by T. A. Davis et al. (2022; see their Section 3.1). The NAI values we obtain are provided in Table A1 and each panel of Figure 4, presenting a gallery of `frank` residual images with the same SNR scale, ordered by increasing NAI.

The disk geometrical parameters, derived from `galario` and subsequently employed in the `frank` fit, are obtained by optimizing a parametric model that assumes fixed values for inclination, PA, and R.A. and decl. offsets for each disk. As `galario` minimizes the difference between observed and model intensity at each sampled *uv*-point, the derived geometrical parameters primarily reflect the geometry of the disk region dominating the flux output, namely, the extended disk rather than the inner regions. This is evident in Figure 4, where the most pronounced residuals tend to be concentrated in the inner regions for the majority of sources, leaving larger radii with residuals exhibiting $|\mathrm{SNR}| < 3$.

5. Discussion

5.1. Source-specific Analysis

In this section, we discuss the substructures observed in the continuum emission of each disk in the exoALMA sample. All features are summarized in Table 3. For a detailed comparison between the locations of our annular substructures and the gradients in the azimuthal velocity deviations from Keplerian rotation, we refer to J. Stadler et al. (2025), who investigate whether the origins of the dust rings are linked to pressure variations. Furthermore, we refer to L. Wölfer et al. (2025) for a comprehensive analysis of the dust asymmetries observed in HD 135344B, HD 143006, HD 34282, and MWC 758, comparing them to gas kinematics to explore whether a vortex could be the underlying cause. In addition, we note that the emission from the observed inner disks may originate from nonthermal components, such as free–free or gyrosynchrotron emission of ionized gas in the proximity of the star (see, e.g., A. A. Rota et al. 2024 for HD 135344B and MWC 758 and A. Sierra et al. 2025 for LkCa 15).

AA Tau (Figure 3). We distinguish three distinct pairs of gaps and rings, along with one fainter outer pair (D105–B111). The nonaxisymmetric features and shadows observed in the first ring (B42) align with the findings of R. A. Loomis et al. (2017), who presented 0.″2 angular resolution observations. Notably, we detect residuals in the inner disk, possibly indicating a misalignment between the inner disk and the B42 ring. There is no sign of the dust inner streamers proposed by R. A. Loomis et al. (2017). Based on our data and residuals, a plausible explanation involves a misaligned inner disk casting shadows onto the B42 ring. This results in emission coming from shadowed and geometrically flatter regions, while the brighter areas, receiving more illumination from the central star, exhibit a greater vertical extent.

CQ Tau (Figure 3). Prominent spiral-like nonaxisymmetric features are evident, with two on the northeast side and one on the southwest side. It should be noted that in these cases, the `frank` model, designed for axisymmetric emission, computes an intermediate intensity between the bright nonaxisymmetric structures and the underlying fainter ring emission. This accounts for the pronounced red–blue patterns observed in the residuals. Our data also reveal a faint inner disk with an integrated intensity of ∼200 μJy. This source was previously studied by M. G. Ubeira Gabellini et al. (2019) with lower-resolution 0.″15 ALMA 1.3 mm (Band 6) observations. By comparing these data to hydrodynamical and radiative transfer simulations, the authors concluded that a massive planet with a minimum mass of 6–9 M_{Jup}, located at a distance of 20 au from the central star, can qualitatively reproduce the continuum intensity radial profile. More recently, I. Hammond et al. (2022) found prominent spirals in SPHERE scattered-light images, aligning with the nonaxisymmetries in our images, and proposed the presence of an inner companion responsible for inducing such spirals.

DM Tau (Figure A2). The disk of DM Tau is characterized by a very extended faint emission, reaching $R_{95} = 245$ au. Strong residuals are only located in correspondence with the inner disk and the B24 ring. They are the result of the observed inner disk and B24 ring being slightly shifted by ∼25 mas toward the northwest compared to the center of the extended emission. This offset becomes particularly evident in the polar plots. The center of our axisymmetric model coincides with the center of the extended emission (as proven by the absence of significant residuals beyond the B24 ring), constituting the bulk of the total emission and hence dominating the `galario` fit. A possible interpretation of the observed residuals involves eccentricity effects, such as a companion on an eccentric orbit carving the gap D14. J. Hashimoto et al. (2021) and L. Francis et al. (2022) studied DM Tau with 0.″035 resolution 1.3 mm ALMA data. Interestingly, the outer gap–ring pairs (D72–B90 and D102–B111), recovered by `frank` in our data set, become more evident in their higher angular resolution continuum image. Moreover, we confirm the asymmetry on the west side of the B24 ring, interpreted by Á. Ribas et al. (2024) as a dust wall.

HD 135344B (Figure A2). Within our sample, HD 135344B exhibits the second-highest NAI (0.401; see Figure 4). This is caused by the bright arc in the southern region of the disk contrasting with faint emission on the northern side. The `frank` fit models this structure as a full ring (B78), generating strong positive residuals in the southern region and negative residuals in the northern part. The data polar plot indicates a B51 ring that is not precisely horizontal, suggesting the possibility of either an eccentric ring or an imperfectly retrieved inclination. HD 135344B has been extensively explored with ALMA multiwavelength observations by P. Cazzoletti et al. (2018), who found that the asymmetry is consistent with a dust trap where dust growth has occurred. S. Casassus et al. (2021) presented 1.3 mm observations at a high resolution of 0.″03 but with lower surface brightness sensitivity (0.72 K) compared to our data (0.05 K). Their work revealed a tentative detection of a filament connecting the B51 and B78 rings. We identify strong residuals (SNR > 35) at the same location, specifically, the red residual aligning with the D66 gap in the southwestern region of the image and at an azimuthal angle of approximately −15° in the residual polar plot.

HD 143006 (Figure A3). The continuum emission from this source has been extensively studied as part of the DSHARP large program by L. M. Pérez et al. (2018), utilizing 0.″046 resolution data at 1.3 mm. Even though unresolved in the image and the intensity radial profile, our `frank` model manages to retrieve the first ring at 7 au, consistent with the radial location of 6 ± 1 au found by J. Huang et al. (2018). L. M. Pérez et al. (2018) derived an inclination of 24.°1 for the inner disk and 17.°0 for the outer disk, while our 2D `galario` model includes a single disk inclination retrieved at 18.°7. Our

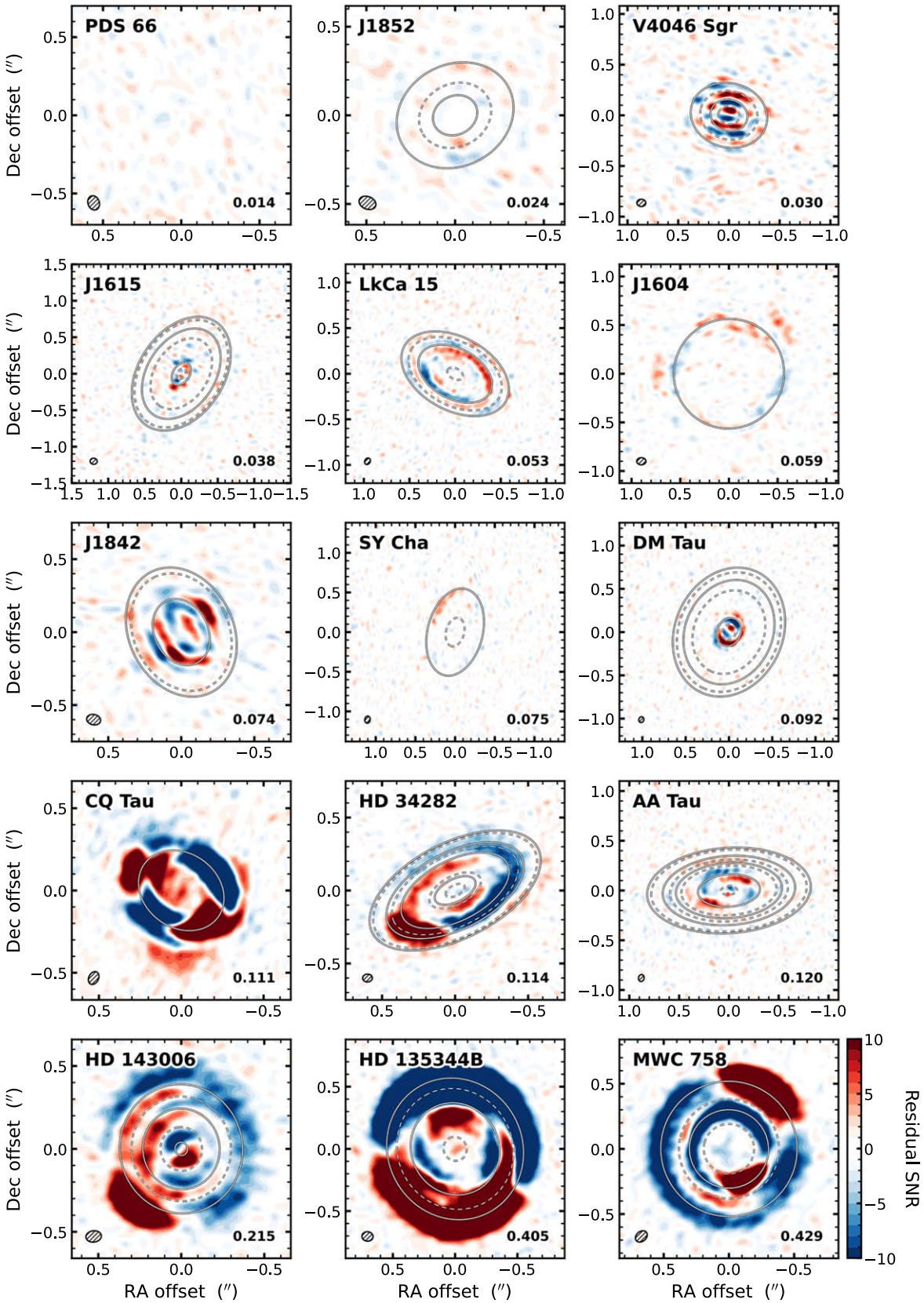

Figure 4. Gallery of residuals plots generated by subtracting the `frank` model (sampled at the same *uv*-points of the observations) from the data and then imaged with CLEAN and robust −0.5. The source order is from the least to the most nonaxisymmetric, according to the NAI presented in Section 4.2 and reported in the lower right corner of each panel and in Table A1. The color scale represents the values of residual SNR in units of the observed noise ($\sigma_{\rm rms}$) for the respective observation, and the same extremes are applied to each plot. Note that the spatial scales are different for every disk. Rings and gaps are marked with solid and dashed ellipses, respectively, while the synthesized beam is indicated by the ellipse in the lower left corner.

Table 3
Summary of the Observed Substructures in Each Disk

Source	Continuum Substructures
AA Tau (Figure 3)	Four gap–ring pairs and an inner disk. Two shadows in the B42 ring with possible elevated surface in the brighter spots. Possible warped inner disk.
CQ Tau (Figure 3)	Inner cavity and one ring with superimposed nonaxisymmetric spiral-like substructures, two on the northeast side and one on the southwest side.
DM Tau (Figure A2)	Inner disk and three pairs of rings and gaps. Offset between the inner disk and the center of the outer disk. Asymmetry on the west side of the B24 ring.
HD 135344B (Figure A2)	Inner cavity with one ring and a bright arc on the southern side. Possible confirmation of the filament connecting the arc with the B51 ring observed by S. Casassus et al. (2021).
HD 143006 (Figure A3)	Inner ring with two pairs of rings and gaps and a bright asymmetry on the southeast side. Eastern side brighter than the western side, consistent with VLT/SPHEREVLT/SPHERE images by M. Benisty et al. (2018). Residuals indicate inner disk misalignment, supporting the warped inner disk interpretation by M. Benisty et al. (2018) and L. M. Pérez et al. (2018).
HD 34282 (Figure A3)	Four gap–ring pairs surrounding an inner cavity and a bright asymmetry on the southeast side. Possible elevated dust surface.
J1604 (Figure A4)	Single ring with an inner cavity. Shadows on the east and west sides of the ring. Possible external gap–ring pair.
J1615 (Figure A4)	Three pairs of rings and gaps with a faint inner disk. Offset between the inner disk and the center of the outer disk.
J1842 (Figure A5)	Inner cavity surrounded by a ring and an additional gap–ring pair. Two shadows in the B36 ring. Signs of an elevated dust surface. Possible external gap–ring pair.
J1852 (Figure A5)	Bright annular ring surrounding an inner cavity hosting a faint ring. Possible point-source feature within the D31 gap.
LkCa 15 (Figure A6)	Two rings surrounding an inner cavity with indications of a third inner ring evident in higher-resolution observations (F. Long et al. 2022; C. H. Gardner et al. 2025). Confirmation of the residuals around the Lagrangian points presented by F. Long et al. (2022). Residuals along the minor axis indicating an elevated dust surface. Presence of a shoulder in the faint outer emission around 170 au.
MWC 758 (Figure A6)	Two rings each with a superimposed bright asymmetry. Eccentric inner cavity with a faint inner disk that is offset from the center of the outer disk.
PDS 66 (Figure A7)	No clear substructures, only a subtle change in the intensity radial profile slope at 45 au.
SY Cha (Figure A7)	Inner disk and one ring with an extended outer shoulder. Bright asymmetry on the northern side of the ring.
V4046 Sgr (Figure A8)	Inner disk and two rings, with the outer one having extended external emission. Offset between the inner disk and the center of the outer disk.

residuals around the inner ring might be an effect of the inner ring misalignment proposed by M. Benisty et al. (2018) and L. M. Pérez et al. (2018). In addition, we observe a general pattern in our residuals where the eastern side is brighter than the western side, a feature that is also evident in the data image. This closely resembles the pattern observed in the Very Large Telescope (VLT) SPHERE images from M. Benisty et al. (2018), which revealed a large-scale shadow on the western side, presumably caused by the warped inner disk. Our observations confirm these findings and further support the hypothesis of a misaligned inner disk. However, our residuals do not fully recover the spiral pattern indicated in the work of S. M. Andrews et al. (2021), possibly due to their different approach, where they excised the large-scale asymmetry before fitting with `frank` and did not use a parametric fit with `galario` to estimate the offsets in R.A. and decl. between the disk center and the observation phase center. Additionally, G. Ballabio et al. (2021) propose the presence of a strongly inclined binary and an outer planetary companion by comparing their simulations to the morphologies observed in the dust continuum and gas channel maps with ALMA, as well as NIR scattered light with VLT/SPHERE.

HD 34282 (Figure A3). Our `frank` model identifies a faint inner disk and three gap–ring pairs, which were not resolved in the lower-resolution (∼0.″14) Band 7 ALMA observations presented by G. van der Plas et al. (2017). The relevant nonaxisymmetric feature to the southeast of the disk generates the negative residuals as a counterpart due to the axisymmetric nature of the `frank` fit. Red residuals along the minor axis may indicate an elevated dust surface, with a morphology consistent with the disk inclination derived from gas data, where the northeast side is the far side (M. Galloway-Sprietsma et al. 2025).

J1604 (Figure A4). We detect the presence of the shadows on the east and west sides of the B82 ring that were previously identified by S. Mayama et al. (2018) and J. Stadler et al. (2023) with angular resolutions of ∼0.″2 at 0.9 mm and ∼0.″05 at 1.3 mm, respectively, using ALMA observations. The high sensitivity of our data also allows us to reveal, in both the data and the `frank` model intensity radial profiles, the presence of a potential new external pair of gap and ring, situated beyond R_{90} and therefore not included in our classification of annular substructures. The gap is located at 139.5 au (0.″965) and the ring at 148.1 au (1.″024). The external ring in the `frank` profile has a peak SNR of ∼14 with respect to the observed azimuthally averaged noise level at the same radius. We refer to C. T. Yoshida et al. (2025) for a detailed analysis of J1604, including a multiwavelength continuum study and a comparison with the retrieved gas surface density.

J1615 (Figure A4). Similarly to DM Tau, this source presents the inner disk and the first B26 ring slightly shifted by ∼20 mas to the southeast from the center of the outer disk, producing the visible residuals. Lower-resolution data of J1615 were presented in N. van der Marel et al. (2015), but with our observation, we can resolve a total of three pairs of gaps and rings.

J1842 (Figure A5). This disk exhibits two shadows within the emission of the B36 ring (particularly evident in the image with the linear stretch in Figure A1) and shows clear signs of an elevated dust emission surface. In particular, the emission just inside the B36 ring on the west side of the cavity appears to originate from the inner edge of a vertically extended cavity wall. Gas kinematics data (M. Galloway-Sprietsma et al. 2025) confirm that the west side of the disk corresponds to the far side. Moreover, the residual pattern, with alternating red and blue residuals along the minor axis, is consistent with the

expected residuals obtained by applying a flat model (as `frank` does) to an elevated emission surface, as illustrated in Appendix A of S. M. Andrews et al. (2021). However, we note that this interpretation does not align with the pattern proposed by Á. Ribas et al. (2024). According to their work, an exposed inner cavity would result in a locally brighter emission, which is not observed in J1842. A possible explanation for this disagreement could be the presence of an inner disk (not detected in the continuum emission), which might prevent the cavity wall from receiving direct illumination from the central star. Additionally, this inner disk could also be responsible for the observed shadows. In addition to the gap–ring pair D63–B70, the `frank` model retrieves another pair beyond R_{90}. The gap is estimated to be at 98.1 au (0.″650) and the ring at 105.6 au (0.″700). Differently from J1604, in this case, the substructures are visible only in the `frank` profile and not in the azimuthally averaged profile of the CLEAN image. Therefore, we exercise caution regarding the presence of this particular gap–ring pair.

J1852 (Figure A5). The source is composed by the ring B50, and then both the azimuthally averaged CLEAN intensity radial profile and the `frank` model resolve the faint inner ring B19 inside the cavity. Notably, this inner ring was predicted by M. Villenave et al. (2019), who performed a radiative transfer model to match the SPHERE data, spectral energy distribution, and low-resolution ALMA data for this disk. Their model produced a prediction for an ALMA image before convolution presenting a faint inner ring, also suggesting a possible composition of small dust grains with low millimeter opacity. In addition to the faint inner ring, an intriguing feature emerges both in the image data and in the residuals, located at gap D31 on the southern side of the disk. The feature has a significance of $\sim 5\sigma$ (with σ being the rms noise in the image) and is situated adjacent to a negative residual with the same significance, tracing a small region where the observed B50 ring emission contracts compared to the `frank` model. Future higher-resolution observations are required to inspect the nature of this feature and determine whether it is genuine or an artifact.

LkCa 15 (Figure A6). We recover with a significance of 3σ–4σ the residuals around the Lagrangian points previously studied by F. Long et al. (2022) using $\sim$0.″05 resolution images at 0.9 and 1.3 mm. We also identify pronounced residuals along the minor axis, resembling the residuals presented in S. Facchini et al. (2020). This could be indicative of emission coming from a geometrically thick ring (see also J. Huang et al. 2020). Moreover, both the azimuthally averaged CLEAN intensity radial profile and the `frank` model present a shoulder in the extended emission at $\sim$170 au. For a comprehensive study of the origins of the observed dust and gas substructures in LkCa 15, combining higher-resolution observations and comparing with numerical simulations, see C. H. Gardner et al. (2025). Moreover, note that at higher resolution, an inner ring (B43) becomes visible, while with our resolution, it does not meet the criteria defining annular substructures (Section 4.1).

MWC 758 (Figure A6). The disk of MWC 758 has the highest NAI value in our sample (0.429; see Figure 4). The `frank` model identifies an inner disk and then two gap–ring pairs. This disk has been extensively studied, e.g., by R. Dong et al. (2018) with 0.″04 resolution ALMA observations at 0.9 mm. Their work revealed the eccentricity of the central cavity and indicated that the spirals observed in NIR scattered light (M. Benisty et al. 2015) align with the continuum asymmetries.

PDS 66 (Figure A7). This source stands out in the exoALMA sample as the only one that does not exhibit substructures in the continuum emission. All residuals show a significance of less than 4σ. `frank`, however, only identifies a subtle change in slope in the intensity radial profile at 45 au. Recently, PDS 66 was analyzed by Á. Ribas et al. (2023) with multiwavelength ALMA observations. Their 1.3 mm observations at 0.″05 resolution also reveal a smooth disk. Our measured R_{68} and R_{90} align perfectly with the estimates made by Á. Ribas et al. (2023) using data at 1.3 and 2.2 mm, indicating a consistent dust continuum extent between 0.9 and 2.2 mm observing wavelengths. This provides additional evidence for optically thick emission at these wavelengths, where gaps, rings, and other substructures would be challenging to detect unless they involve a very large depletion or concentration of material, as the emission would primarily trace the uniform surface of the disk.

SY Cha (Figure A7). Our data identify an inner disk in the middle of a cavity surrounded by the B101 ring and an extended fainter emission reaching an R_{95} of 228.1 au. The B101 ring shows a nonaxisymmetric feature on its northern side. This structure reflects what was observed by R. Orihara et al. (2023) using ALMA observations at 1.3 mm at 0.″04 resolution.

V4046 Sgr (Figure A8). This disk exhibits both an inner disk and the first B13 ring shifted by $\sim$27 mas to the north relative to the center of the outer disk, akin to the cases of DM Tau and J1615. This causes the alternating red–blue residuals, evident also in the residual polar plot. This system hosts a tight binary system (G. R. Quast et al. 2000), and the gas emission is very smooth (C. Pinte et al. 2025). A possible explanation of the observed morphology might be a misalignment of the inner binary, causing the formation of two dust rings as proposed by H. Aly & G. Lodato (2020) and C. Longarini et al. (2021). However, this is challenging given the system's tight binary configuration, presenting a semimajor axis of $\approx$0.041 au (corresponding to an orbital period of 2.42 days) in a circular orbit ($e \leqslant 0.01$) and stars with very similar masses ($0.90 \pm 0.05\,M_{\odot}$ and $0.85 \pm 0.05\,M_{\odot}$; G. R. Quast et al. 2000; K. A. Rosenfeld et al. 2012). Additionally, if there were a misalignment, the dynamical mass derived from the disk would be inconsistent with the one derived from the binary orbit, as noted by K. A. Rosenfeld et al. (2012). Another hypothesis could involve an eccentric planet within the D8 gap. No local perturbations are identified in the gas channel maps (C. Pinte et al. 2025), but, interestingly, J. Stadler et al. (2025) detect a negative gradient in the ^{12}CO azimuthal velocity deviation from Keplerian rotation colocated with the B13 ring, indicating that the ring just outside the D8 gap is consistent with a dust trap. Higher-resolution continuum observations of V4046 Sgr at 1.3 mm, as presented by R. Martinez-Brunner et al. (2022) and P. Weber et al. (2022), reveal similar structures, although the offset of the inner disk is less pronounced.

5.2. Inner–Outer Disk Connection

The definition of the NAI (see Section 4.2) is valuable for quantifying the morphological characteristics of each disk and investigating potential explanations by identifying patterns with other properties of the disk and its central star. The left

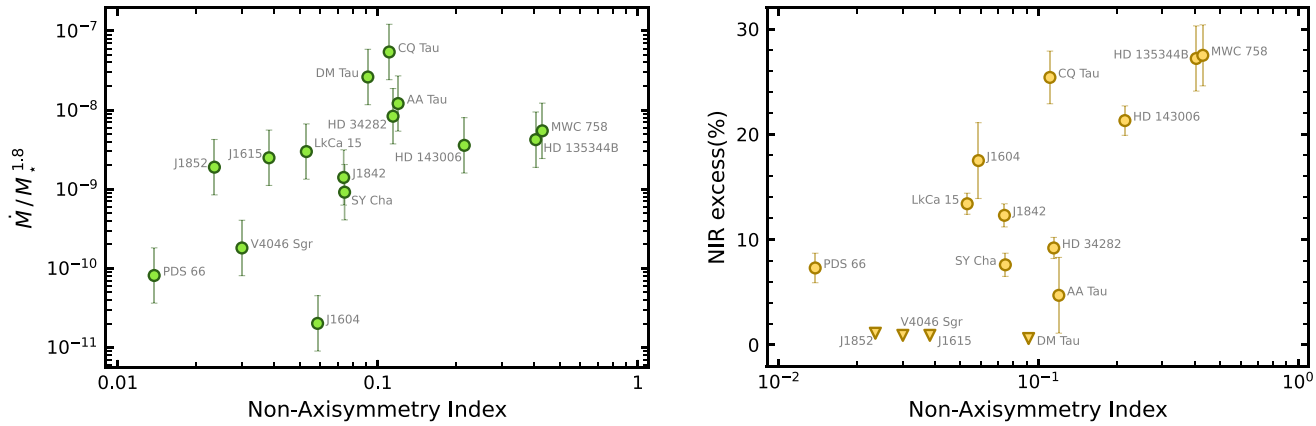

Figure 5. Mass accretion rate and NIR excess as function of the NAI (higher values indicating more asymmetric disks). Left plot: log–log plot of the mass accretion rate, normalized for the correlation with the stellar mass assuming $\dot{M} \propto M_\star^{1.8}$ (C. F. Manara et al. 2023), as a function of the NAI (defined in Section 4.2). Right panel: lin–log plot of NIR excess vs. the NAI. Downward-pointing triangles represent upper limits. Values of the NIR excess are reported in Table D1.

plot of Figure 5 presents the mass accretion rate versus the NAI. The mass accretion rate $\dot{M}$ scales with the stellar mass $M_\star$ following a steeper-than-linear relation $\dot{M} \propto M_\star^\gamma$ with $\gamma \sim 1.6$–2 (compilation by C. F. Manara et al. 2023). To homogeneously compare the mass accretion rates across the 15 disks in our sample, we normalized the mass accretion rate to account for its dependence on the stellar mass by considering $\dot{M}/M_\star^{1.8}$, assuming $\gamma = 1.8$. This value is plotted on the y-axis of the left panel in Figure 5.

The relation between the measured NIR excess of each disk and the corresponding NAI is presented in the right plot of Figure 5, where the NIR excess quantifies the excess flux in the NIR above the stellar photosphere, typically tracing hot dust in the inner disk. For some disks, we report the NIR excess from A. Garufi et al. (2018). For sources not included in that work, the NIR excess was calculated following the same procedure, namely, integrating the dereddened flux measured by the Two Micron All Sky Survey and Wide-field Infrared Survey Explorer photometry from 1.2 to 4.5 μm in excess over a Phoenix model of the stellar photosphere (P. H. Hashimoto et al. 1999) with the $T_{\rm eff}$ of the specific source. The final value is then normalized to the total stellar flux. Values of the mass accretion rate and NIR excess are reported in Appendix D and Table D1.

The Kendall's tau coefficient for the relation between the mass accretion rate (normalized for stellar mass dependence) and the NAI is 0.45 with a p-value of 0.02, while for the relation between NIR excess and the NAI, it is 0.48 with a p-value of 0.01. Both indicate moderate, statistically significant positive correlations. We verified that assuming an exponent of 1.6 or 2 for the normalization of the mass accretion rate to stellar mass yields minimal differences, as well as completely omitting the normalization to stellar mass (see Figure E1). Figure E2 in Appendix E shows the correlations between stellar mass from `discminer` (A. F. Izquierdo et al. 2025) and dust disk mass, calculated as explained in Section 2, with NAI. A weak correlation between dust disk mass and NAI is observed (Kendall's tau coefficient of 0.31 with a p-value of 0.11). In contrast, for stellar mass and NAI, while the Kendall's tau test suggests no significant correlation (0.10 with a p-value of 0.62), the plot interestingly shows that the most asymmetric sources are also the ones with higher stellar masses. While our findings are robust within the exoALMA sample, it is important to note that the sample selection may introduce biases that influence these results, as it primarily targets bright, extended disks with significant substructures. Future studies with a more diverse sample could help confirm these trends.

Each plot clearly shows that the most asymmetric sources also exhibit the highest values of accretion rate and NIR excess. Interestingly, of the six most nonaxisymmetric disks in our sample (CQ Tau, HD 34282, AA Tau, HD 143006, HD 135344B, and MWC 758, all with NAI > 0.1), five exhibit inner cavities. A. Garufi et al. (2018) analyzed a substantial NIR data set on protoplanetary disks, concluding that the presence of spirals and shadows is associated with a high NIR excess. Our results align with their findings, as NIR spirals often coincide with strong nonaxisymmetric features in the millimeter dust continuum emission. A plausible explanation for this involves a massive perturber generating the NIR spirals, such as a stellar or planetary companion within the observed cavities in our most asymmetric sources, potentially triggering higher mass accretion onto the central star. Future theoretical and numerical work should explore this possibility in greater detail.

5.3. Presence of Companions

In this section, we explore the possibility of companions, either stellar or planetary, in the disks of our sample. This analysis is first carried out by comparing the observed continuum substructures with numerical simulations from the literature, followed by assessing correspondences with gas kinematic signatures from exoALMA ^{12}CO observations presented by C. Pinte et al. (2025). Our findings suggest that while massive companions could explain some observed substructures, such as central cavities and major asymmetries, no clear evidence of direct companion emission is found in the continuum data. The comparison with gas kinematic data yields mixed conclusions, with some continuum substructures aligning with kinematic signatures, while others do not provide conclusive evidence.

In Section 5.2, we propose that massive companions (either stellar or planetary) may plausibly explain why the most asymmetric disks with higher NAI values tend to have a central inner cavity and higher mass accretion rates and NIR excess. This interpretation is supported by the work of J. Calcino et al. (2023), who define criteria linking gas kinematic asymmetries and central cavities to the presence of inner binaries.

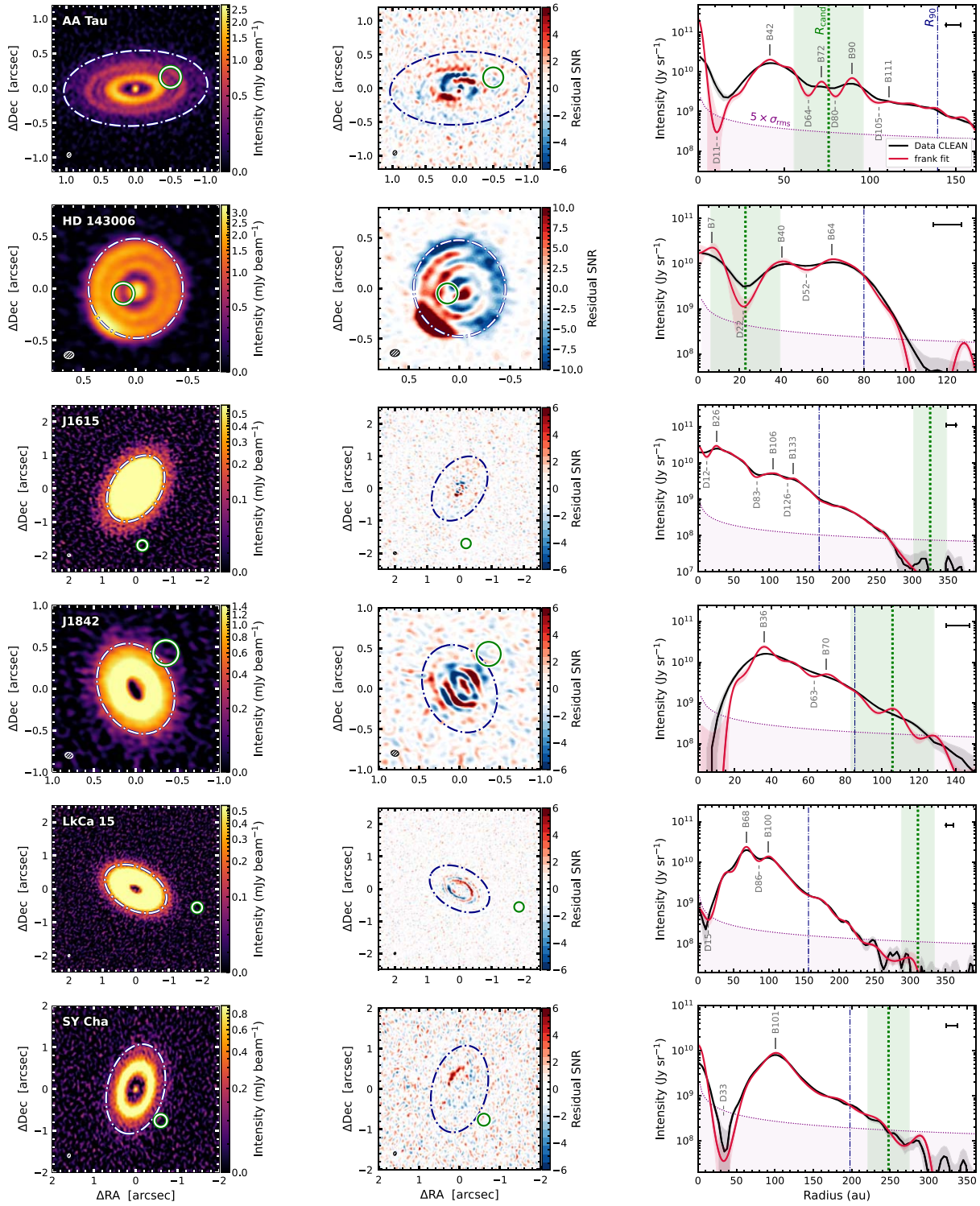

Figure 6. Comparison between the continuum emission and the ^{12}CO velocity kinks identified by C. Pinte et al. (2024). The left panels show the continuum emission from the fiducial CLEAN data images, and the middle panels display the `frank` residuals. Dashed–dotted ellipses represent R_{90}, while solid circles indicate the positions of the velocity kinks, deprojected onto the midplane. Ellipses in the lower left corner indicate the synthesized beam. The right panels show the intensity radial profile of the azimuthally averaged fiducial CLEAN images (black) and the `frank` model (red). Vertical blue dashed–dotted lines represent R_{90}, while the vertical green dotted lines indicate the radial location deprojected onto the midplane of the planet candidates generating the kinks ($R_{\rm cand}$). The green shaded area in the intensity profile and the size of the green circles in the 2D images represent the uncertainty due to the gas image beam size (C. Pinte et al. 2025). The purple shaded area represents intensity values below 5 times the rms noise ($\sigma_{\rm rms}$) measured in the CLEAN image.

Regarding planetary companions, J. Speedie et al. (2022) used synthetic ALMA Band 7 observations from hydrodynamic and radiative transfer simulations to show how thermal mass planets at tens of astronomical units can drive spirals in the dust continuum emission, which are effectively highlighted in residual maps. However, they note that gaps and rings can obscure spirals by limiting the disk area where spirals are visible. Furthermore, J. A. Sturm et al. (2020) demonstrated

Table 4
Continuum Outer Disk Fit

Source	λ_{out} (au)	$\sigma_{fit}/\sigma_{beam}$	R_{gas}/R_{dust}
(1)	(2)	(3)	(4)
AA Tau	22.6 ± 1.0	4.9	$3.18^{+0.40}_{-0.37}$
CQ Tau	11.9 ± 0.4	2.9	$2.33^{+1.37}_{-0.76}$
DM Tau	70.3 ± 9.7	10.7	$3.89^{+0.16}_{-0.14}$
HD 135344B	6.8 ± 0.1	2.1	$2.17^{+0.33}_{-0.18}$
HD 143006	6.5 ± 0.2	1.4	$1.83^{+0.62}_{-0.46}$
HD 34282	52.3 ± 0.8	6.3	$2.50^{+0.34}_{-0.20}$
J1604	13.0 ± 0.3	2.5	$2.09^{+0.10}_{-0.09}$
J1615	48.5 ± 1.3	7.1	$2.98^{+0.18}_{-0.14}$
J1842	16.4 ± 0.6	3.0	$3.29^{+0.52}_{-0.34}$
J1852	9.9 ± 0.3	2.1	$3.21^{+0.61}_{-0.40}$
LkCa 15	32.4 ± 1.3	6.6	$4.47^{+0.27}_{-0.20}$
MWC 758	6.3 ± 0.2	1.5	$2.91^{+0.55}_{-0.33}$
PDS 66	6.1 ± 0.2	1.9	$2.39^{+0.70}_{-0.47}$
SY Cha	37.7 ± 1.3	4.8	$2.74^{+0.31}_{-0.28}$
V4046 Sgr	10.9 ± 0.6	4.2	$5.47^{+0.36}_{-0.35}$

Note. Column (1): target name. Column (2): scale length of the outer disk taper λ_{out} from the exponential model $I(R) = I_0 \exp[-R/\lambda_{out}]$. Column (3): ratio between the σ_{fit} from the Gaussian model $I(R) = A \exp[-(x - R_{90})^2/2\sigma^2_{fit}]$ and the σ_{beam} obtained by averaging the major and minor axis σ values of the synthesized beam. Column 4: ratio between R_{90} from ^{12}CO (M. Galloway-Sprietsma et al. 2025) and from the dust continuum (Table 2).

that planet-induced spirals in the dust are significantly weaker than those in the gas, with the amplitude of the dust spirals decreasing with higher Stokes numbers.

In our sample, apart from the spiral-like asymmetries in CQ Tau, no disks exhibit clear full spirals in the dust continuum. While crescent-shaped features are observed and known to sometimes coincide with spirals in the NIR (see Figure 1 in L. Wölfer et al. 2025), our residuals show no unambiguous spiral structures. The only spiral-like feature in the `frank` residuals (Figure 4) is seen in DM Tau, but as detailed in Section 5.1, we interpret this as an artifact caused by the offset between the inner disk and the first bright ring relative to the outer disk center. This lack of clear spiral structures prevents us from inferring planetary companions solely from continuum morphology.

Additional insights come from comparing the continuum substructures to the work of C. Pinte et al. (2025), who analyzed ^{12}CO data cubes from exoALMA and identified six disks with kinematic signatures consistent with planet wakes: AA Tau, HD 143006, J1615, J1842, LkCa 15, and SY Cha. The kink locations deprojected to the midplane are compared with our continuum morphologies in Figure 6. Given the difficulties in assigning a robust uncertainty to the kink location, we estimate the uncertainty using the gas image beam size (C. Pinte et al. 2025). Specifically, in the data images and residuals, the kink locations are marked with circles centered at the deprojected kink positions, with a radius equal to the gas beam size. In the intensity radial profiles, the radial locations of the planet candidates generating the kinks (R_{cand}) are indicated with green dashed lines, while the associated uncertainties are represented by green shaded areas spanning $R_{cand} \pm$ one gas beam size. We found no evidence of direct emission that could be interpreted as coming from a companion, either in the fiducial images or in the `frank` residuals. However, valuable observations can be made by comparing the candidate locations to the substructures in the intensity radial profiles.

For AA Tau, the kink aligns with the D80 gap, further supporting the hypothesis of a planetary companion carving this gap. In HD 143006, they detected hints of the same kink observed in DSHARP data, potentially explained by a giant planet located within the continuum D22 gap (L. M. Pérez et al. 2018; C. Pinte et al. 2020; G. Ballabio et al. 2021). For J1615 and LkCa 15, the kinematic candidates are situated at distances where both the azimuthally averaged CLEAN image and the `frank` profile fall below the noise level. However, as noted by C. Pinte et al. (2025), it is interesting to observe that the locations of these candidates lie just outside the region where the dust emission drops, potentially hinting that these candidates could be truncating the disk. In J1842, the proposed kink is located beyond R_{90} but still has SNR > 5 in the azimuthally averaged intensity radial profile. In this region, the `frank` profile reveals substructures not visible in the azimuthally averaged intensity radial profile from the CLEAN image. In SY Cha, the candidate location corresponds to a region beyond R_{90} where both the azimuthally averaged CLEAN profile and the `frank` model identify a gap at ∼270 au, followed by a slight increase in intensity and a sharp drop at ∼300 au. This outer gap–ring pair has an SNR ranging from 2 to 5. Despite the low SNR, the correspondence between the candidate location and these outer substructures could suggest a candidate carving a gap and creating a faint ring in the disk outer region.

Finally, we aim to provide a flux density upper limit for the undetected circumplanetary disks (CPDs). For AA Tau and HD 143006, where the kink location corresponds to a dust gap, a statistical approach would be necessary, with an injection-recovery test to characterize CPDs in residual images, as done in S. M. Andrews et al. (2021). This is because pixels in the gaps are highly correlated, and nonaxisymmetric residuals can still influence the estimate. This would be best approached with a dedicated study that can invest more effort into asymmetric models of the circumstellar material. However, we can straightforwardly provide a flux density upper limit for the remaining four disks, where the kink location is beyond R_{90}. The (3σ) upper limit on the emission is derived as 3 times the rms measured in the radial range [R_{cand} − gas beam size, R_{cand} + gas beam size], that is, from an aperture centered on the putative companion location, with a width accounting for the gas beam size. The computed flux density upper limits are 111 μJy for J1615, 312 μJy for J1842, 105 μJy for LkCa 15, and 165 μJy for SY Cha.

5.4. Analysis of the Extended Emission

So far, we characterized the dust emission within R_{90} (see the criteria for defining axisymmetric substructures in Section 4.1). However, the high surface brightness sensitivity of our data set also allows us to inspect the faint outer disk continuum emission. As seen in the intensity radial profiles in Figure 2, there is a region beyond R_{90} with a clear signal before noise becomes dominant at even larger radii. In this region, the azimuthally averaged profile from the CLEAN images and the frank fit are usually in good agreement. These are areas where we detect a reliable signal that is not visible in the CLEAN images but is revealed in the profiles due to the azimuthal average boosting the local SNR.

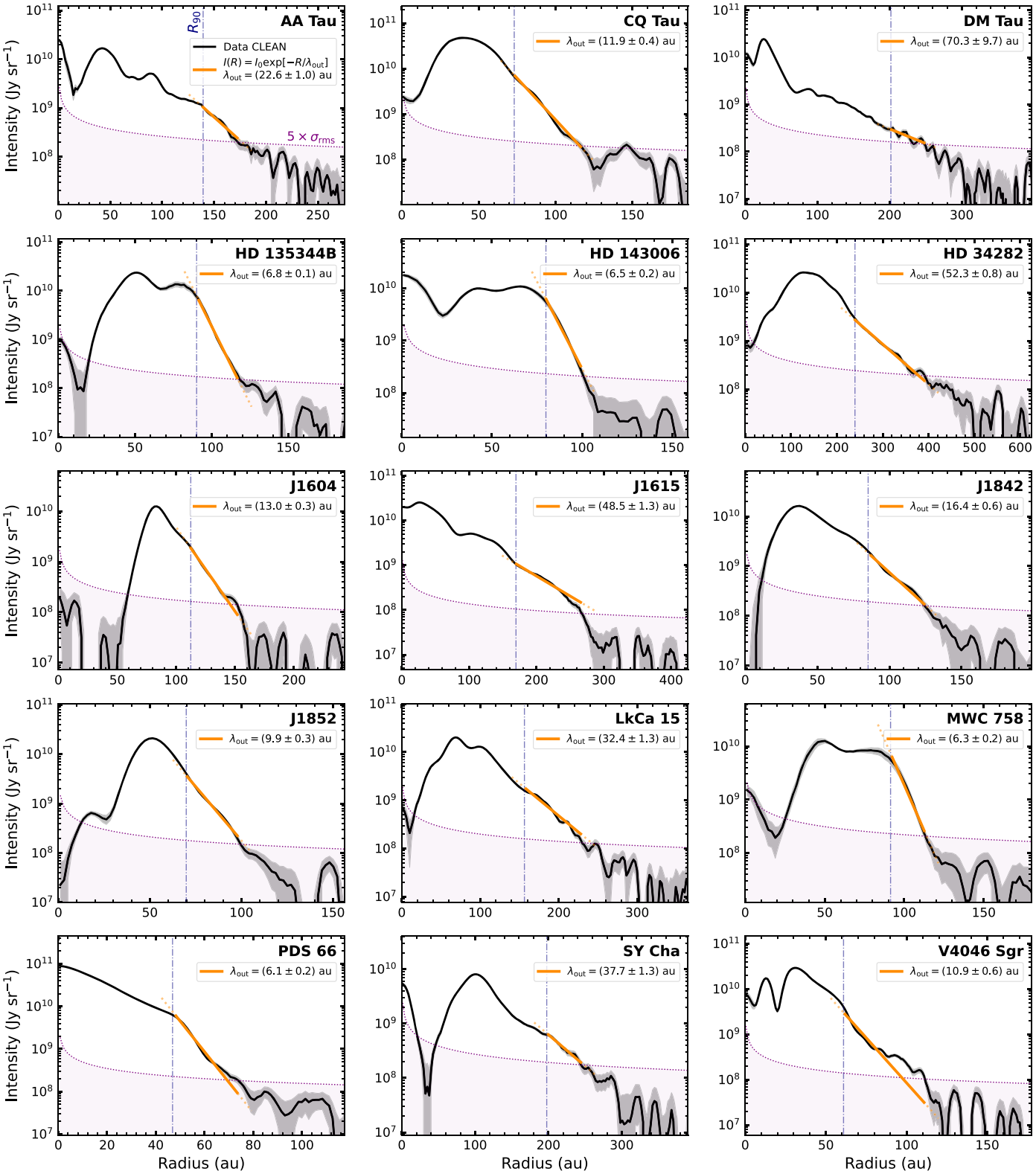

Figure 7. Gallery showing the fits of the continuum extended emission with an exponential function in a log-lin scale. The intensity radial profiles are from the azimuthally averaged CLEAN images with robust −0.5. The blue vertical dashed–dotted line indicates R_{90}, while the purple shaded area represents intensity values below 5 times the rms noise σ_{rms} measured in the CLEAN image. The rms noise is properly scaled accounting for the radial dependence of the azimuthal average, that is, dividing the σ_{rms} by the square root of the number of beams within the corresponding radial annulus. The orange line shows the best fit using the exponential model $I(R) = I_0 \exp[-R/\lambda_{out}]$ of the region between R_{90} and the radius where the intensity intersects the $5 \times \sigma_{rms}$ line.

We also note that in our data, the continuum flux density in these outer regions is robustly recovered without the maximum recoverable scale being a limiting factor. This is because exoALMA was primarily designed to study gas emission, which extends beyond the dust continuum emission (see column (4) in Table 4). To capture large-scale structures, the

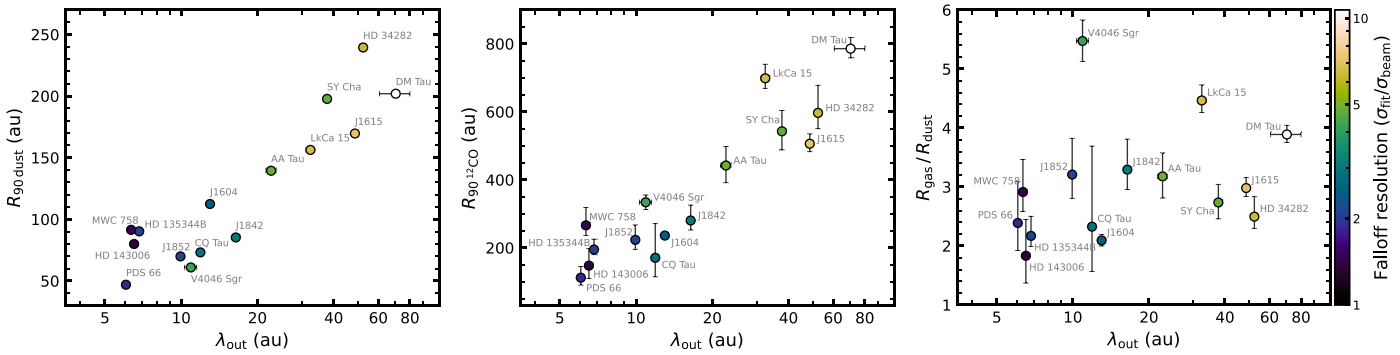

Figure 8. From left to right: radius enclosing 90% of the continuum emission ($R_{90\ \mathrm{dust}}$), radius enclosing 90% of the ^{12}CO emission ($R_{90\ ^{12}\mathrm{CO}}$; M. Galloway-Sprietsma et al. 2025), and their ratio ($R_{\mathrm{gas}}/R_{\mathrm{dust}}$) as a function of the parameter λ_{out} from the exponential model of the continuum extended emission $I(R) = I_0 \exp[-R/\lambda_{\mathrm{out}}]$. Uncertainties on $R_{90\ \mathrm{dust}}$ are present but smaller than the data points. The color scale indicates the number of beams resolving the outer disk falloff, with values of $\sigma_{\mathrm{fit}}/\sigma_{\mathrm{beam}}$ (Table 4) displayed on a logarithmic scale.

observations combine a compact ALMA configuration and, for the most extended sources, also include the ACA.

To quantitatively characterize this continuum's outer regions, considering only the azimuthally averaged CLEAN profile, we focus on the radius range beyond R_{90} and out to where the intensity is above 5 times the rms noise. Within this radial range, the intensity profiles appear generally linear in a log-lin plot. Therefore, we fitted these regions with an exponential function:

$$I(R) = I_0 \exp\left[-\frac{R}{\lambda_{\mathrm{out}}}\right]. \quad (7)$$

The parameter λ_{out} represents the scale length of the outer disk emission taper, with higher values indicating a flatter outer disk. Figure 7 presents a gallery with the results of these fits for each exoALMA source. We observe that the exponential function well reproduces the overall intensity profile trend in the outer regions for most of the disks. It only partially fails in the case of V4046 Sgr, which does not exhibit a single slope.

To determine whether we have sufficient angular resolution to accurately resolve the steepness of the extended emission, we first fitted the same radial range with a Gaussian model centered on R_{90}, i.e.,

$$I(R) = A \exp\left[-\frac{(x - R_{90})^2}{2\sigma_{\mathrm{fit}}^2}\right]. \quad (8)$$

Next, we divided σ_{fit} by σ_{beam}, which is the average of the σ values of the major and minor axes of the synthesized beam. Values of γ and $\sigma_{\mathrm{fit}}/\sigma_{\mathrm{beam}}$ are listed in Table 4. We consider the descent to be resolved if $\sigma_{\mathrm{fit}}/\sigma_{\mathrm{beam}} > 2$. Thus, the steepness of HD 143006, MWC 758, and PDS 66 is not resolved.

In Figure 8, we present R_{90} from the continuum emission, the ^{12}CO emission, and their ratio as a function of the parameter λ_{out} from the exponential model. The color scale represents the number of beams resolving the outer disk falloff, showing values of $\sigma_{\mathrm{fit}}/\sigma_{\mathrm{beam}}$ on a logarithmic scale. These plots illustrate that larger disks (both in dust and in gas) within our sample systematically have a shallower slope in the falloff of their outer regions, whereas more compact disks exhibit a steeper outer edge. The steepness may be even greater for sources whose outer descent we are not fully resolving. On the other hand, there is no correlation between the ratio of the gas and dust radii and the λ_{out} parameter. Therefore, even though dust radial drift could play an important role in shaping the outer disk continuum falloff, it is not straightforward to establish this connection with the current findings. Other phenomena that might directly influence the appearance of the faint outer disk emission include late infall events or disk truncation caused by flybys or outer companions. Additionally, it is worth noting that a metric like the one presented here has not been included in theoretical studies examining disk size in dust with and without substructures (e.g., G. P. Rosotti et al. 2019; A. Zormpas et al. 2022; L. Delussu et al. 2024). Future modeling efforts could benefit from exploring this metric in more detail.

6. Conclusions

In this Letter, we analyzed the continuum emission from the ALMA Band 7 data of the 15 disks in the exoALMA Large Program. In the quest to understand the origin of the observed dust morphologies, we characterized both the axisymmetric and nonaxisymmetric substructures, as well as the bright inner regions and faint outer regions of each disk.

We developed a pipeline focused on visibility fitting to characterize axisymmetric substructures (rings and gaps) and nonaxisymmetric residuals obtained by subtracting an axisymmetric model from the data.

1. Our procedure begins with a parametric fit using the code `galario` (M. Tazzari et al. 2018) to retrieve solid estimates of the geometrical parameters (inclination, PA, offsets in R.A. and decl.). These parameters are then employed in a nonparametric fit with the package `frank` (J. Jennings et al. 2020), resulting in a superresolution 1D best-fit model of the radial intensity profile.
2. We use the `frank` model intensity profile to define the radial location, width, and depth of rings and gaps, limiting this characterization within R_{90}. Next, we use the same axisymmetric model to extract nonaxisymmetric residuals from the data. We define the NAI as a measure to quantify the level of asymmetry for each disk.

Our main findings are summarized below. It should be noted that these results have been obtained from a biased sample of large and bright disks. Future, more complete surveys will be essential to determine whether these findings hold for the broader population of protoplanetary disks.

1. The data angular resolution and sensitivity allowed us to retrieve specific features for the various disks. These include prominent shadows (AA Tau, HD 143006, J1604, J1842), inner disks offset with respect to the outer disk center (DM Tau, J1615, V4046 Sgr), possible warped inner disks (AA Tau, HD 143006), indications of a dust wall (J1842) and a geometrically thick disk (AA Tau, HD 34282, LkCa 15), potential external substructures (an outer ring in J1604 and J1842 and an outer shoulder in LkCa 15), and a seemingly structureless disk (PDS 66).
2. Except for PDS 66, all other disks in our sample exhibit some form of nonaxisymmetric features. Only CQ Tau hosts clear spiral-like structures, while five disks (HD 135344B, HD 143006, HD 34282, MWC 758, and SY Cha) show crescent-shaped asymmetries. The remaining eight disks present other types of irregularities. This suggests that, given sufficient angular resolution and sensitivity, nonaxisymmetries may be a common characteristic of protoplanetary disks.
3. In our attempt to gain a deeper understanding of the origin of the observed strong asymmetries, we found tentative correlations between the NAI and mass accretion rate and NIR excess. Notably, the more asymmetric disks almost all feature inner cavities and consistently exhibit higher values of these parameters. This finding suggests a connection between the outer disk structures and the inner disk properties.
4. Capitalizing on the high surface brightness sensitivity of our data, we provided a preliminary characterization of the continuum extended emission. This outer emission can generally be reproduced with an exponential fit. We found that larger disks exhibit a shallower falloff in the outer regions, while more compact disks present a sharper outer edge.

The data and disk parameters presented in this Letter provided as a publicly available value-added data product. These include CLEAN images of the continuum data and the residuals from the `frank` fit at different robust values, intensity radial profiles from the fiducial CLEAN images and the `frank` fits, radial locations of gaps and rings, geometrical parameters from `galario` (i, PA, ΔR.A., Δdecl.), and values of the continuum radii (R_{68}, R_{90}, R_{95}).

Acknowledgments

The authors thank the anonymous referee for the thorough and detailed review, which greatly helped improve the manuscript. This Letter makes use of the following ALMA data: ADS/JAO.ALMA#2021.1.01123.L. ALMA is a partnership of ESO (representing its member states), NSF (USA) and NINS (Japan), together with NRC (Canada), MOST and ASIAA (Taiwan), and KASI (Republic of Korea), in cooperation with the Republic of Chile. The Joint ALMA Observatory is operated by ESO, AUI/NRAO and NAOJ. The National Radio Astronomy Observatory is a facility of the National Science Foundation operated under cooperative agreement by Associated Universities, Inc. We thank the North American ALMA Science Center (NAASC) for their generous support including providing computing facilities and financial support for student attendance at workshops and publications.

P.C. thanks Antonio Garufi for providing the NIR excess values for the exoALMA sources and Laura Pérez, Anibal Sierra, Enrique Macías, Francesco Zagaria, and María Jesús Mellado for helpful discussions.

P.C. acknowledges support by the Italian Ministero dell'Istruzione, Università e Ricerca through the grant Progetti Premiali 2012-iALMA (CUP C52I13000140001) and by the ANID BASAL project FB210003. S.F. is funded by the European Union (ERC, UNVEIL, 101076613), and acknowledges financial contribution from PRIN-MUR 2022YP5ACE. J.B. acknowledges support from NASA XRP grant No. 80NSSC23K1312. M.B., D.F., J.S, and A.W. have received funding from the European Research Council (ERC) under the European Union's Horizon 2020 research and innovation program (PROTOPLANETS, grant agreement No. 101002188). Computations by J.S. have been performed on the "Mesocentre SIGAMM" machine, hosted by Observatoire de la Cote d'Azur. M.F. has received funding from the European Research Council (ERC) under the European Unions Horizon 2020 research and innovation program (grant agreement No. 757957). M.F. is supported by a grant-in-aid from the Japan Society for the Promotion of Science (KAKENHI: No. JP22H01274). C.H. acknowledges support from NSF AAG grant No. 2407679. J.D.I. acknowledges support from an STFC Ernest Rutherford Fellowship (ST/W004119/1) and a University Academic Fellowship from the University of Leeds. A.I. acknowledges support from the National Aeronautics and Space Administration under grant No. 80NSSC18K0828. Support for A.F.I. was provided by NASA through the NASA Hubble Fellowship grant No. HST-HF2-51532.001-A awarded by the Space Telescope Science Institute, which is operated by the Association of Universities for Research in Astronomy, Inc., for NASA, under contract NAS5-26555. G.L. has received funding from the European Research Council (ERC) under the European Union Horizon 2020 research and innovation program (Grant agreement no. 815559 (MHDiscs)). G.L. and C.L. have received funding from the European Union's Horizon 2020 research and innovation program under the Marie Sklodowska-Curie grant agreement No. 823823 (DUSTBUSTERS). C.L. acknowledges support from the UK Science and Technology Research Council (STFC) via the consolidated grant ST/W000997/1. C.P. acknowledges Australian Research Council funding via FT170100040, DP18010423, DP220103767, and DP240103290. D.P. acknowledges Australian Research Council funding via DP18010423, DP220103767, and DP240103290. G.R. acknowledges funding from the Fondazione Cariplo, grant No. 2022-1217, and the European Research Council (ERC) under the European Union's Horizon Europe Research & Innovation Programme under grant agreement No. 101039651 (DiscEvol). F.M. received funding from the European Research Council (ERC) under the European Union's Horizon Europe research and innovation program (grant agreement No. 101053020, project Dust2Planets). N.C. has received funding from the European Research Council (ERC) under the European Union Horizon Europe research and innovation program (grant agreement No. 101042275, project StellarMADE). L.T. acknowledges funding from Progetti Premiali 2012 iALMA (CUP C52I13000140001), Deutsche Forschungs-gemeinschaft (German Research Foundation) reference No. 325594231 FOR 2634/1 TE 1024/1-1, European Union's Horizon 2020 research and innovation program under the Marie Sklodowska-Curie grant No. 823823 (DUSTBUSTERS), and the ERC via the ERC Synergy grant ECOGAL

(grant No. 855130). T.C.Y. acknowledges support by Grant-in-Aid for JSPS Fellows JP23KJ1008. H.-W.Y. acknowledges support from the National Science and Technology Council (NSTC) in Taiwan through grant NSTC 113-2112-M-001-035- and from the Academia Sinica Career Development Award (AS-CDA-111-M03). G.W.F. acknowledges support from the European Research Council (ERC) under the European Union Horizon 2020 research and innovation program (grant agreement No. 815559 (MHDiscs)). G.W.F. was granted access to the HPC resources of IDRIS under the allocation A0120402231 made by GENCI. Support for B.Z. was provided by The Brinson Foundation. Views and opinions expressed by ERC-funded scientists are, however, those of the author(s) only and do not necessarily reflect those of the European Union or the European Research Council. Neither the European Union nor the granting authority can be held responsible for them.

Appendix A
Supplementary Table and Figures

Table A1 presents all the substructure properties for each disk. Figure A1 shows a gallery of the continuum emission from the exoALMA sample with a linear stretch in the color scale. Figures A2, A3, A4, A5, A6, A7, and A8 complete the disk-specific results gallery introduced in Section 4.2.

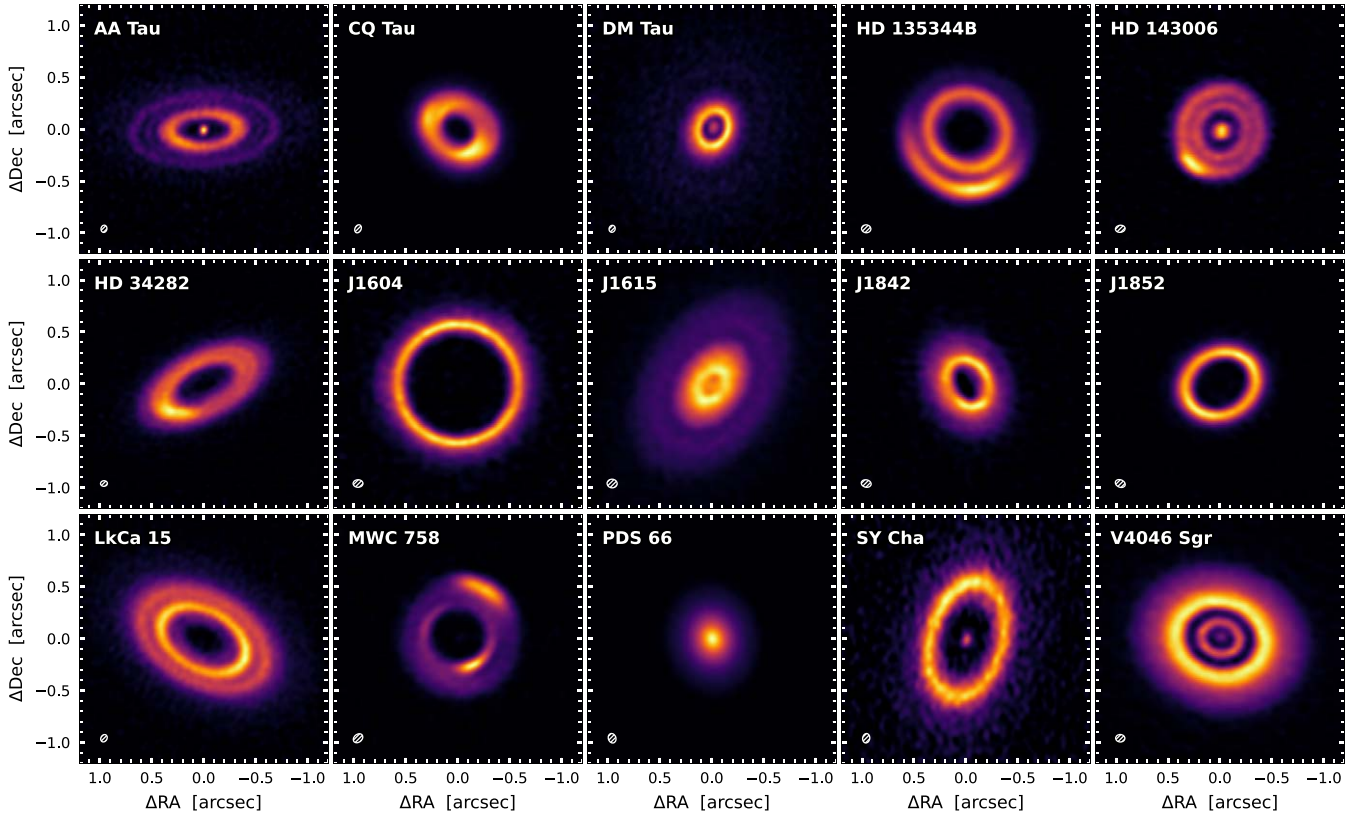

Figure A1. Same as in Figure 1 but with a linear stretch in the color scale to highlight the changes in intensity within the brightest regions.

Table A1
Properties of the Continuum Substructures

Source	Feature	Radial Location (au, arcsec)	Width (au, arcsec)	R_{in} (au, arcsec)	R_{out} (au, arcsec)	Depth	NAI
(1)	(2)	(3)	(4)	(5)	(6)	(7)	(8)
AA Tau	D11	11.0, 0.082	28.1, 0.209	4.9, 0.037	33.0, 0.245	0.01	0.120
	B42	42.0, 0.312	22.8, 0.169	33.0, 0.245	55.8, 0.414	⋯	
	D64	64.3, 0.478	8.2, 0.061	60.3, 0.448	68.5, 0.508	0.44	
	B72	71.8, 0.533	6.8, 0.051	68.5, 0.508	75.3, 0.559	⋯	
	D80	79.8, 0.593	10.2, 0.076	75.3, 0.559	85.5, 0.635	0.34	
	B90	89.8, 0.666	8.7, 0.065	85.5, 0.635	94.2, 0.699	⋯	
	D105	105.3, 0.782	4.9, 0.036	103.1, 0.766	108.0, 0.802	0.94	
	B111	110.9, 0.823	6.0, 0.044	108.0, 0.802	114.0, 0.846	⋯	
CQ Tau	B41	41.2, 0.276	33.4, 0.223	26.1, 0.175	59.5, 0.398	⋯	0.111
DM Tau	D14	13.5, 0.094	12.7, 0.088	7.7, 0.053	20.4, 0.142	0.08	0.092
	B24	24.1, 0.167	10.7, 0.074	20.4, 0.142	31.1, 0.216	⋯	
	D72	71.8, 0.498	18.7, 0.130	64.4, 0.447	83.1, 0.577	0.78	

Table A1
(Continued)

Source	Feature	Radial Location (au, arcsec)	Width (au, arcsec)	R_{in} (au, arcsec)	R_{out} (au, arcsec)	Depth	NAI
(1)	(2)	(3)	(4)	(5)	(6)	(7)	(8)
	B90	89.5, 0.622	10.6, 0.074	83.1, 0.577	93.7, 0.651	⋯	
	D102	102.4, 0.712	6.6, 0.046	99.2, 0.689	105.8, 0.735	0.92	
	B111	110.6, 0.768	9.4, 0.065	105.8, 0.735	115.2, 0.800	⋯	
HD 135344B	D13	13.2, 0.098	40.8, 0.302	1.5, 0.011	42.3, 0.313	0.0	0.405
	B51	50.8, 0.376	17.3, 0.128	42.3, 0.313	59.6, 0.441	⋯	
	D66	66.4, 0.493	11.4, 0.084	60.9, 0.451	72.3, 0.535	0.47	
	B78	78.1, 0.578	13.6, 0.101	72.3, 0.535	85.9, 0.636	⋯	
HD 143006	B7	6.6, 0.040	5.4, 0.033	3.6, 0.022	9.0, 0.055	⋯	0.215
	D22	21.8, 0.132	18.3, 0.111	13.8, 0.084	32.1, 0.195	0.1	
	B40	40.3, 0.244	12.6, 0.076	32.1, 0.195	44.7, 0.271	⋯	
	D52	52.2, 0.316	13.8, 0.084	44.7, 0.271	58.5, 0.354	0.58	
	B64	64.4, 0.390	12.9, 0.078	58.5, 0.354	71.4, 0.433	⋯	
HD 34282	D22	21.8, 0.071	26.8, 0.087	8.8, 0.029	35.6, 0.115	0.2	0.114
	B47	46.8, 0.152	16.9, 0.055	35.6, 0.115	52.5, 0.170	⋯	
	D59	59.3, 0.192	44.4, 0.144	52.5, 0.170	96.9, 0.314	0.1	
	B124	124.4, 0.403	42.7, 0.138	96.9, 0.314	139.7, 0.453	⋯	
	D145	145.2, 0.470	12.0, 0.039	139.7, 0.453	151.7, 0.492	0.96	
	B158	157.7, 0.511	9.6, 0.031	151.7, 0.492	161.3, 0.523	⋯	
	D188	188.2, 0.610	5.7, 0.018	186.2, 0.603	191.9, 0.622	0.96	
	B196	196.4, 0.637	7.0, 0.023	191.9, 0.622	198.9, 0.645	⋯	
J1604	B82	82.1, 0.568	9.5, 0.066	78.0, 0.539	87.6, 0.606	⋯	0.059
J1615	D12	12.3, 0.079	14.0, 0.090	5.4, 0.035	19.3, 0.124	0.49	0.038
	B26	25.9, 0.167	15.7, 0.101	19.3, 0.124	35.0, 0.225	⋯	
	D83	82.6, 0.531	14.1, 0.090	76.7, 0.493	90.8, 0.583	0.77	
	B106	105.6, 0.679	23.3, 0.150	90.8, 0.583	114.1, 0.733	⋯	
	D126	125.5, 0.807	6.3, 0.040	122.8, 0.789	129.0, 0.829	0.97	
	B133	132.9, 0.854	6.2, 0.040	129.0, 0.829	135.3, 0.869	⋯	
J1842	B36	35.8, 0.237	14.0, 0.092	30.2, 0.200	44.2, 0.293	⋯	0.074
	D63	63.2, 0.419	5.9, 0.039	60.6, 0.402	66.5, 0.440	0.87	
	B70	69.7, 0.461	5.9, 0.039	66.5, 0.440	72.4, 0.480	⋯	
J1852	B19	19.0, 0.129	7.2, 0.049	15.6, 0.106	22.8, 0.155	⋯	0.024
	D31	30.9, 0.210	22.3, 0.152	22.8, 0.155	45.2, 0.307	0.01	
	B50	50.0, 0.340	12.3, 0.084	45.2, 0.307	57.5, 0.391	⋯	
LkCa 15	D15	14.6, 0.093	51.4, 0.327	6.8, 0.043	58.2, 0.370	0.02	0.053
	B68	68.2, 0.434	22.9, 0.146	58.2, 0.370	81.1, 0.516	⋯	
	D86	86.3, 0.549	12.0, 0.077	81.1, 0.516	93.2, 0.593	0.76	
	B100	99.5, 0.633	12.7, 0.081	93.2, 0.593	105.9, 0.673	⋯	
MWC 758	D30	30.1, 0.193	38.5, 0.247	4.5, 0.029	43.0, 0.276	0.01	0.429
	B47	47.3, 0.303	10.4, 0.067	43.0, 0.276	53.4, 0.342	⋯	
	D60	59.9, 0.384	8.6, 0.055	56.4, 0.362	65.0, 0.417	0.77	
	B82	81.6, 0.523	21.1, 0.135	65.0, 0.417	86.1, 0.552	⋯	
PDS 66	⋯	⋯	⋯	⋯	⋯	⋯	0.014
SY Cha	D33	33.3, 0.184	74.0, 0.409	7.2, 0.040	81.1, 0.449	0.04	0.075
	B101	101.2, 0.560	39.9, 0.221	81.1, 0.449	121.1, 0.670	⋯	
V4046 Sgr	D8	7.5, 0.105	7.3, 0.101	4.2, 0.059	11.5, 0.161	0.01	0.030
	B13	13.1, 0.184	3.4, 0.047	11.5, 0.161	14.9, 0.208	⋯	
	D20	20.4, 0.285	10.1, 0.141	15.1, 0.211	25.2, 0.352	0.01	
	B27	27.2, 0.380	15.4, 0.216	25.2, 0.352	40.6, 0.568	⋯	

Note. Column (1): target name. Column (2): annular substructure label. "B" (for bright) indicates a ring, while "D" (for dark) indicates a gap. The number in the label is the feature distance from the central star measured in au. Column (3): substructure radial location, extracted as explained in Section 4.1. Column (4): annular substructure width. Columns (5) and (6): inner and outer edge of the substructure. Column (7): gap depth. Substructure width, edges, and gap depth are derived following the criteria of J. Huang et al. (2018). Column (8): NAI, computed as described in Section 4.2.

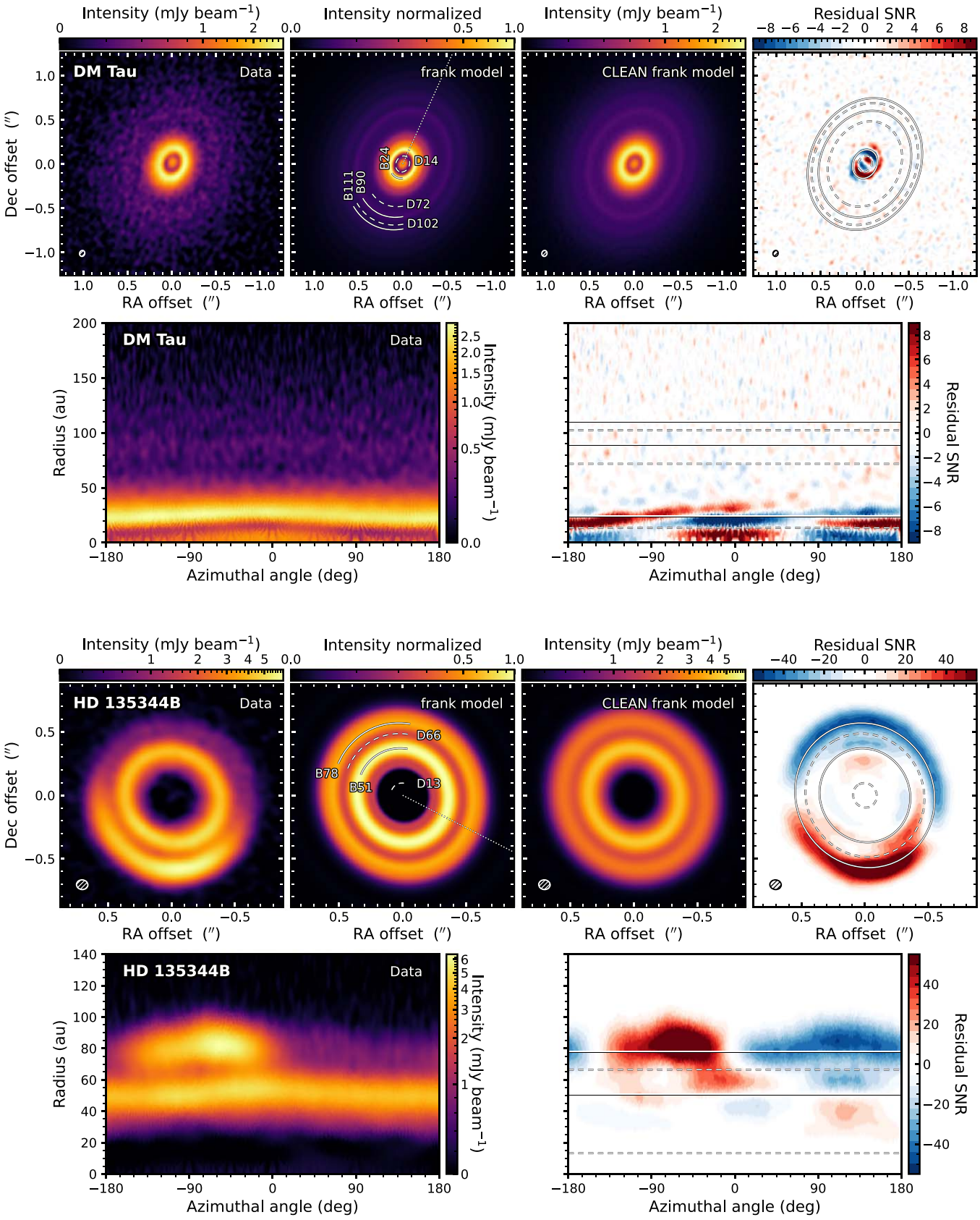

Figure A2. Same as Figure 3 but for DM Tau and HD 135344B.

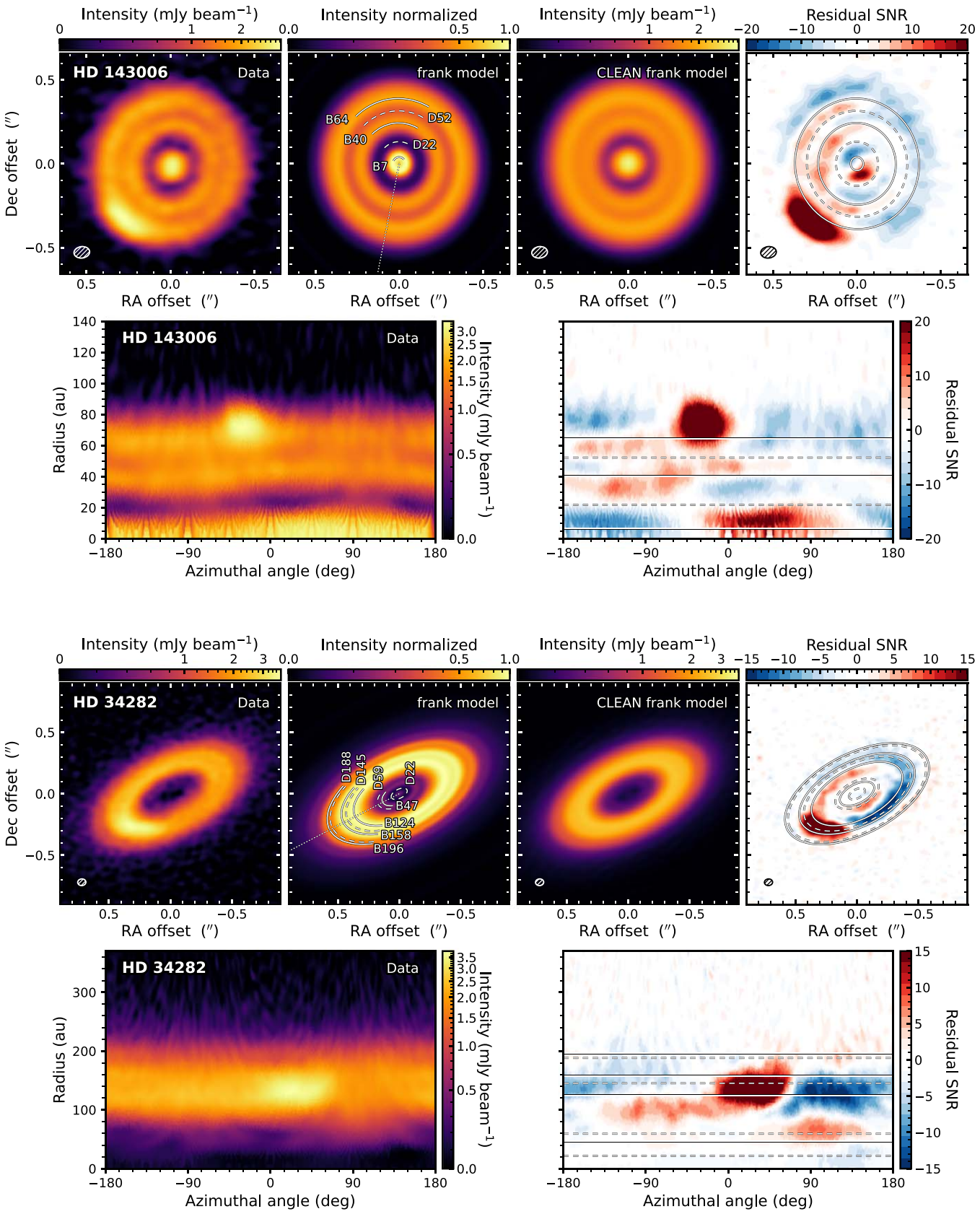

Figure A3. Same as Figure 3 but for HD 143006 and HD 34282.

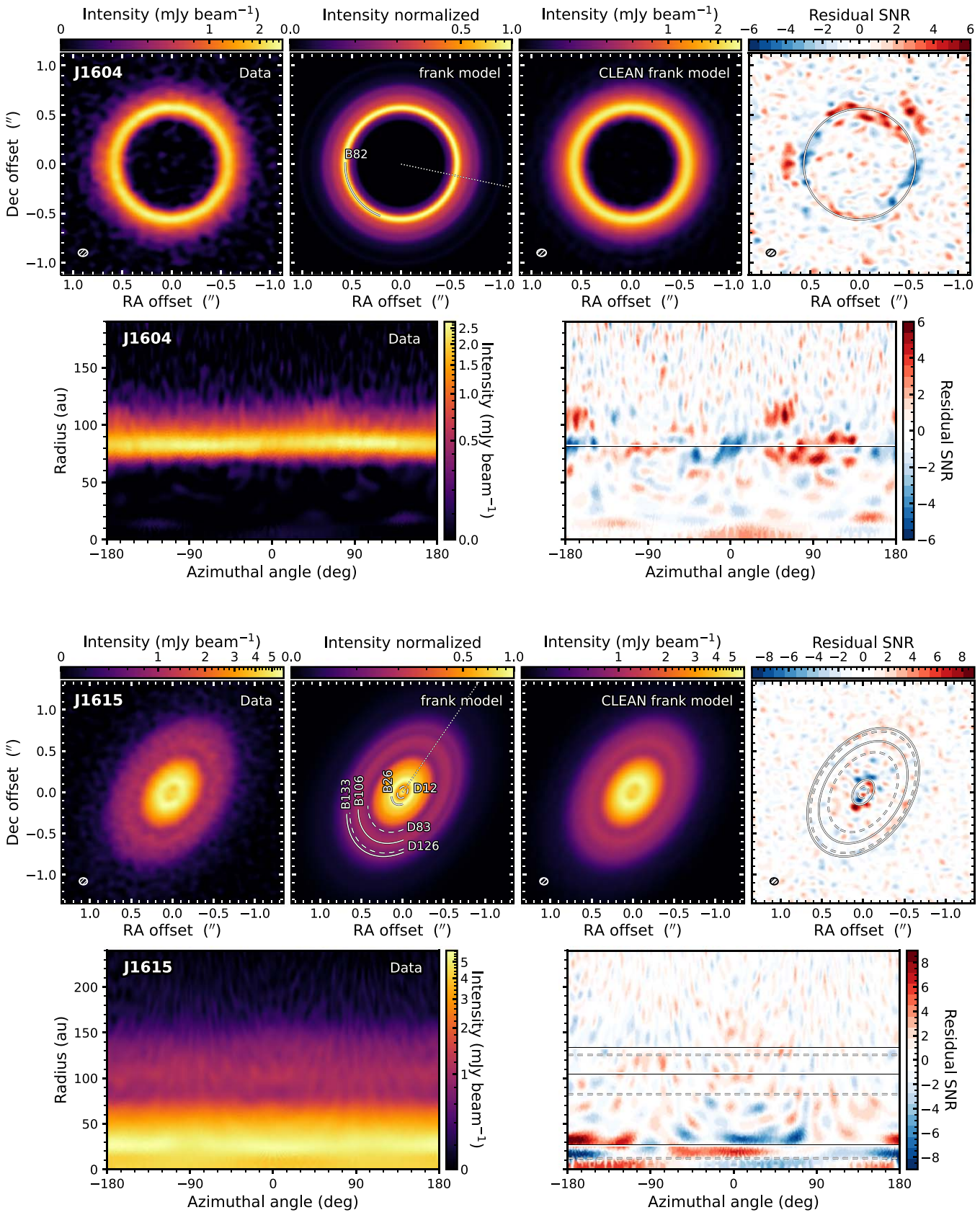

Figure A4. Same as Figure 3 but for J1604 and J1615.

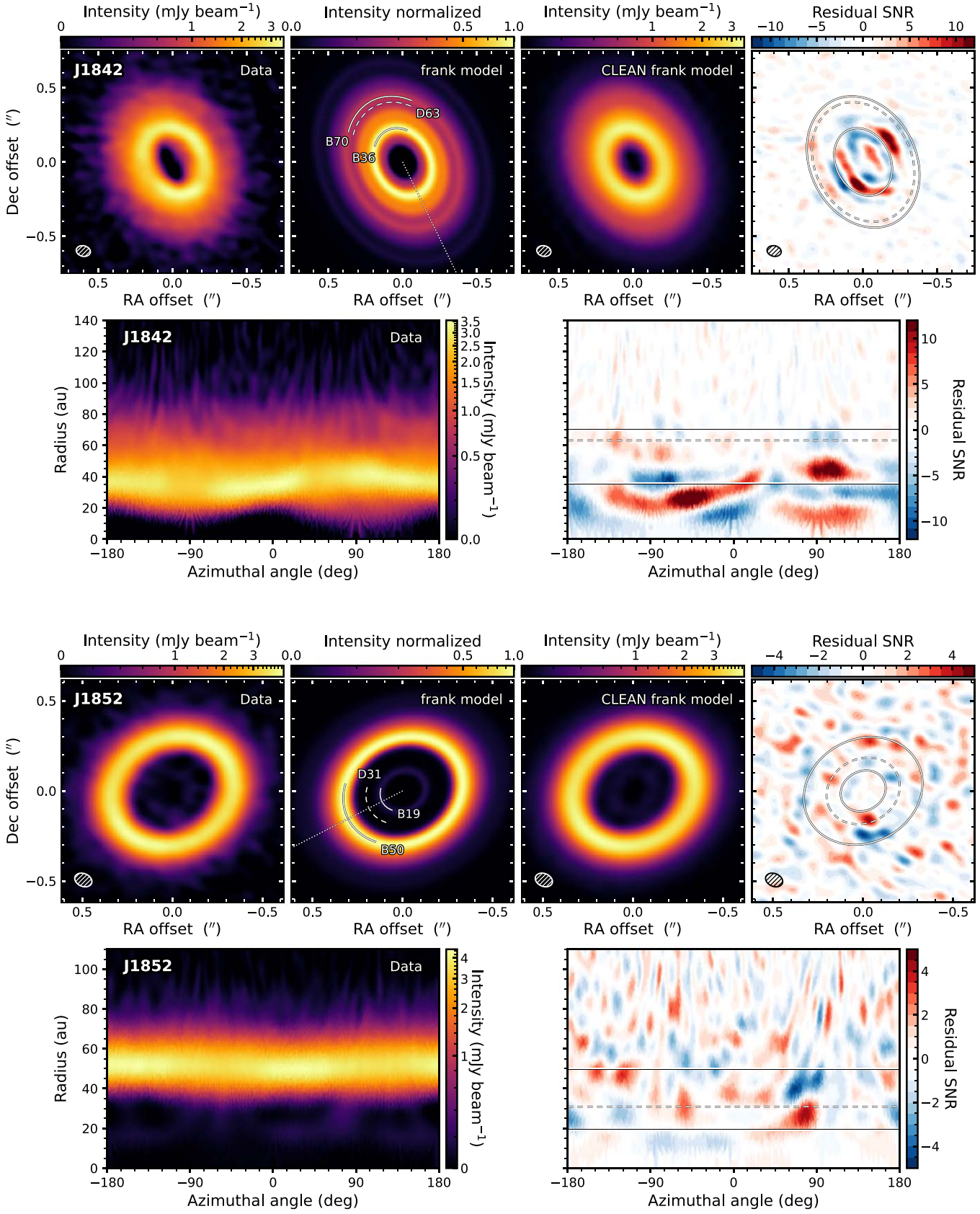

Figure A5. Same as Figure 3 but for J1842 and J1852.

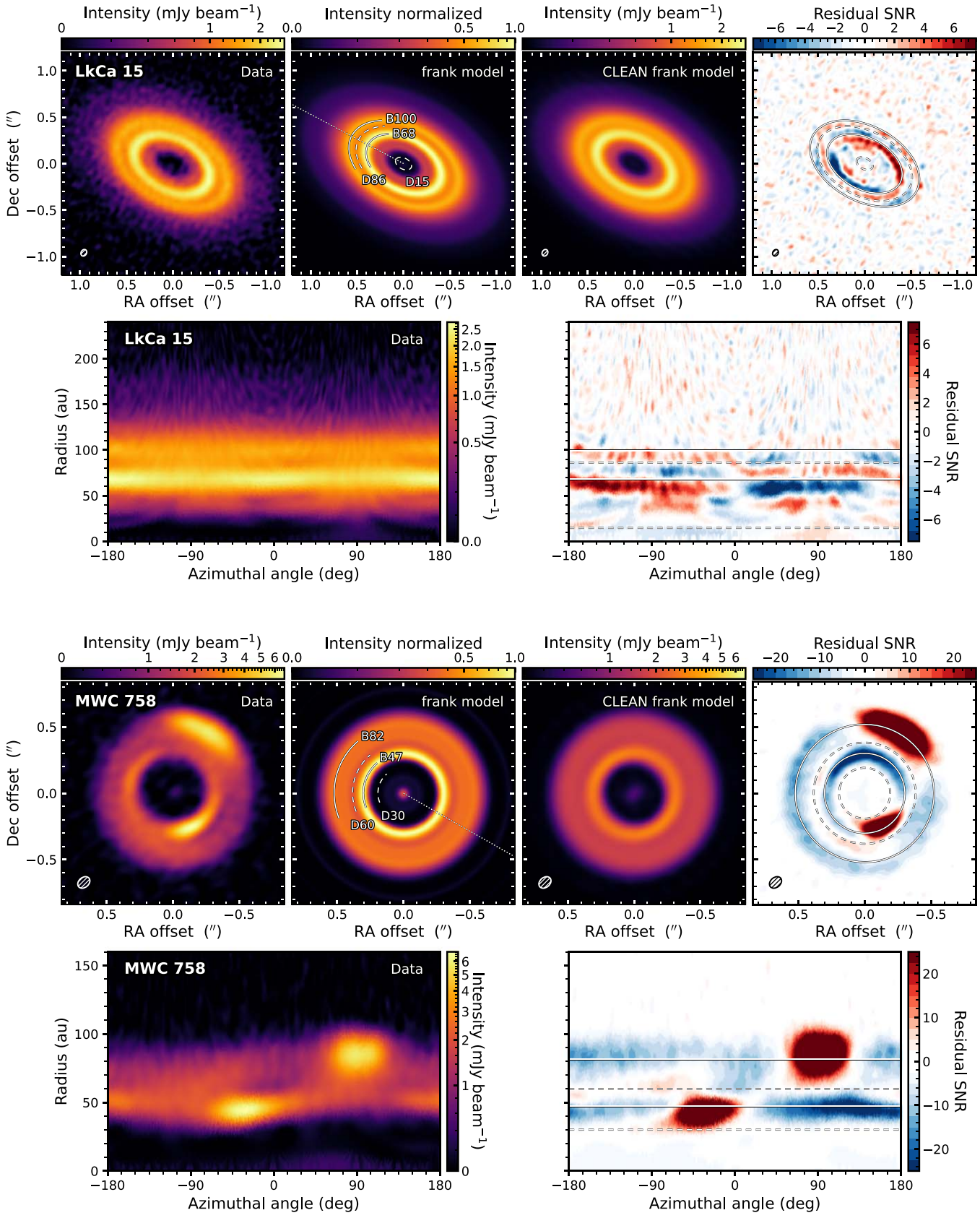

Figure A6. Same as Figure 3 but for LkCa 15 and MWC 758.

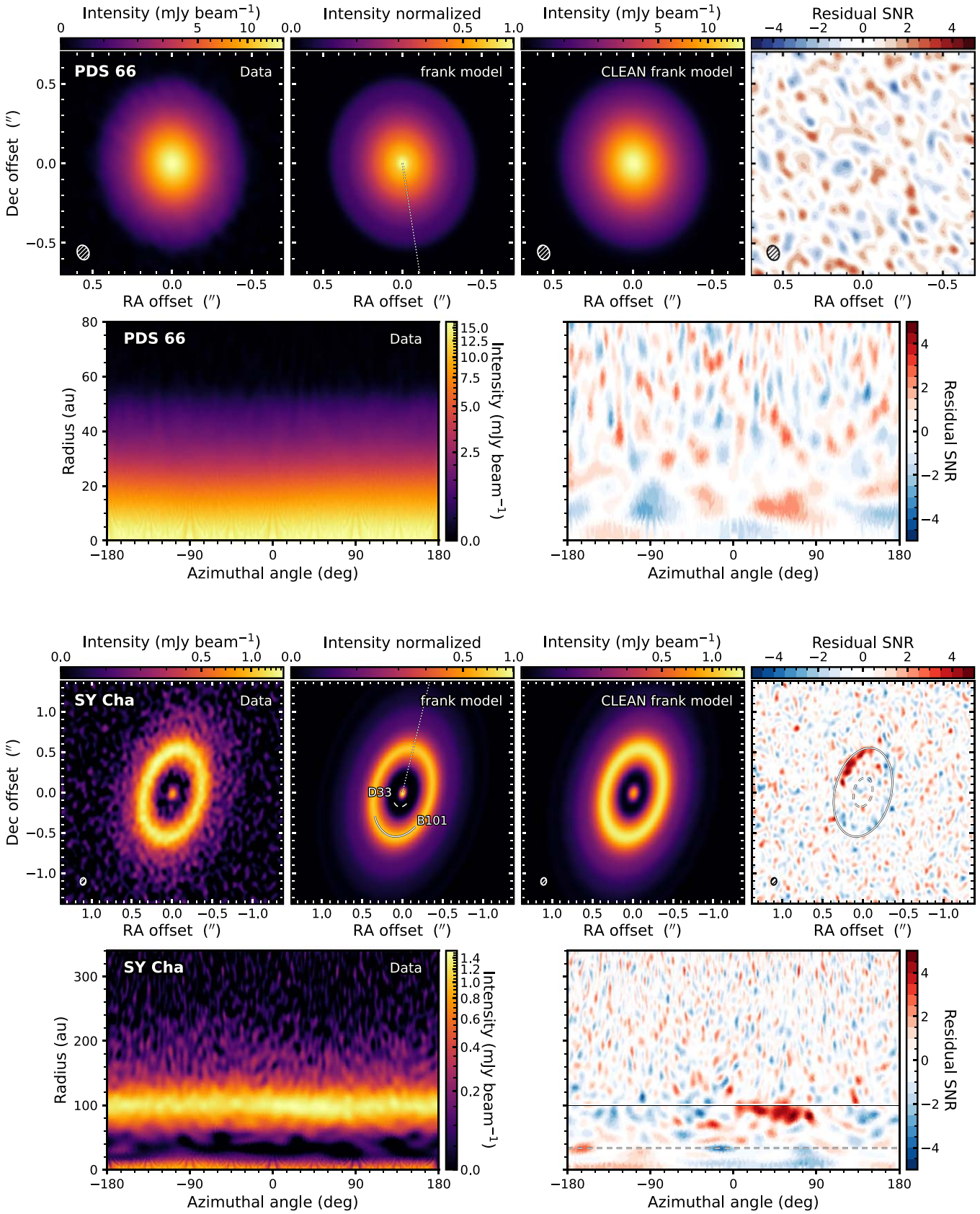

Figure A7. Same as Figure 3 but for PDS 66 and SY Cha.

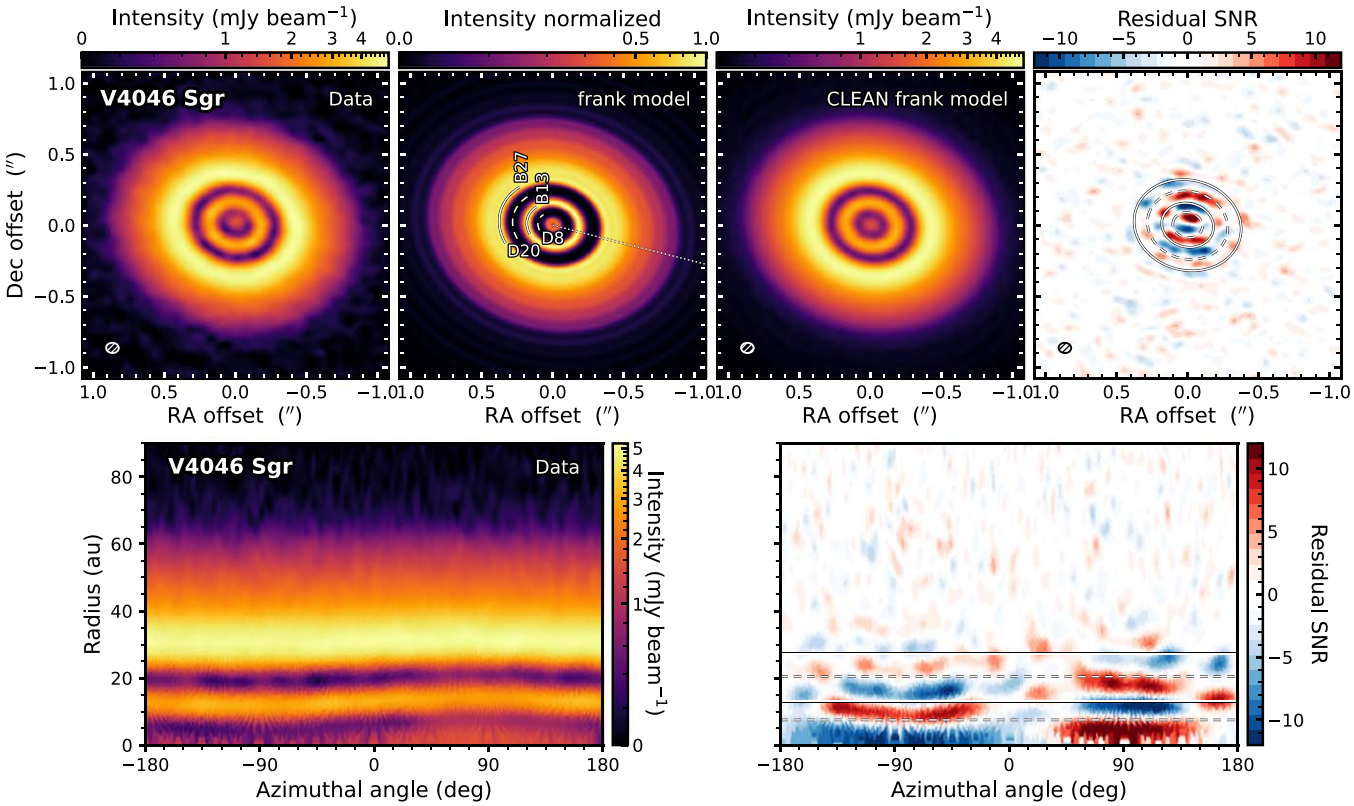

Figure A8. Same as Figure 3 but for V4046 Sgr.

Appendix B
Visibility Modeling

Tables B1 and B2 present the `galario` best-fit results for each parameter in the 1D and 2D parametric models, respectively. Figure B1 displays a gallery of the visibility profiles as a function of deprojected baseline for each source, along with the best-fit profiles from `galario` and `frank`.

Table B1
`galario` Best-fit Results for 1D Parametric Models

Source	Model	Inner disk		Ring		
		$\log_{10}(f)$ (Jy sr^{-1})	σ (mas)	$\log_{10}(f)$ (Jy sr^{-1})	r (mas)	σ (mas)
(1)	(2)	(3)	(4)	(5)	(6)	(7)
AA Tau	Central point source + four rings	$15.444^{+0.003}_{-0.003}$	⋯	$10.11^{+0.01}_{-0.01}$ $9.90^{+0.03}_{-0.03}$ $9.66^{+0.01}_{-0.01}$ $9.524^{+0.003}_{-0.003}$	344^{+2}_{-2} 281^{+1}_{-1} $663.4^{+0.5}_{-0.5}$ 423^{+4}_{-4}	55^{+1}_{-1} 33^{+1}_{-1} $23.0^{+0.9}_{-0.9}$ 387^{+2}_{-2}
DM Tau	Central Gaussian + three rings	$11.5^{+0.1}_{-0.2}$	6^{+1}_{-1}	$10.357^{+0.001}_{-0.001}$ $9.40^{+0.02}_{-0.02}$ $8.71^{+0.06}_{-0.07}$	$192.9^{+0.1}_{-0.1}$ 124^{+14}_{-13} 458^{+111}_{-101}	$57.2^{+0.2}_{-0.2}$ 485^{+8}_{-8} 771^{+25}_{-25}
J1604	Two rings	⋯	⋯	$10.210^{+0.001}_{-0.001}$ $9.546^{+0.002}_{-0.002}$	$572.7^{+0.1}_{-0.1}$ $670.3^{+0.6}_{-0.6}$	$30.5^{+0.2}_{-0.2}$ $108.4^{+0.3}_{-0.3}$
J1615	Central Gaussian + three rings	$8.15^{+0.01}_{-0.06}$	$0.08^{+0.02}_{-0.01}$	$10.3982^{+0.0003}_{-0.0002}$ $9.665^{+0.001}_{-0.001}$ $8.707^{+0.005}_{-0.003}$	$0.1795^{+0.0002}_{-0.0002}$ $0.7122^{+0.0006}_{-0.0006}$ $1.249^{+0.005}_{-0.006}$	$0.1551^{+0.0003}_{-0.0003}$ $0.1882^{+0.0009}_{-0.0008}$ $0.227^{+0.004}_{-0.003}$
J1842	Three rings	⋯	⋯	$10.247^{+0.002}_{-0.002}$ $9.759^{+0.005}_{-0.005}$ $8.77^{+0.03}_{-0.03}$	$242.2^{+0.2}_{-0.2}$ 373^{+2}_{-2} 551^{+14}_{-13}	$47.2^{+0.3}_{-0.3}$ 109.4^{+1}_{-1} 177^{+4}_{-5}
J1852	Three rings	⋯	⋯	$10.456^{+0.001}_{-0.001}$ $9.5^{+0.1}_{-0.2}$ $9.562^{+0.006}_{-0.008}$	$348.9^{+0.2}_{-0.1}$ 134^{+2}_{-3} 430^{+1}_{-1}	$35.1^{+0.2}_{-0.1}$ 6.5^{+3}_{-2} $82.2^{+0.6}_{-0.5}$
LkCa 15	Four rings	⋯	⋯	$10.295^{+0.001}_{-0.001}$ $10.000^{+0.001}_{-0.001}$ $10.69^{+0.02}_{-0.03}$ $9.513^{+0.003}_{-0.004}$	$429.0^{+0.1}_{-0.1}$ $635^{+0.3}_{-0.3}$ $259.5^{+0.1}_{-0.1}$ 606^{+2}_{-2}	$53.7^{+0.1}_{-0.1}$ $88.2^{+0.4}_{-0.4}$ $2.5^{+0.1}_{-0.1}$ 341^{+1}_{-1}
PDS 66	Central Gaussian + one ring	$10.9405^{+0.0004}_{-0.0004}$	$123.8^{+0.4}_{-0.4}$	$10.106^{+0.004}_{-0.003}$	295^{+2}_{-2}	$141.5^{+0.7}_{-0.7}$
SY Cha	Central Gaussian + two rings	$10.2^{+0.04}_{-0.04}$	27^{+2}_{-2}	$9.879^{+0.001}_{-0.001}$ $9.062^{+0.004}_{-0.004}$	$55.6^{+0.4}_{-0.4}$ 747^{+4}_{-4}	$95.1^{+0.4}_{-0.4}$ 326^{+2}_{-2}
V4046 Sgr	Central Gaussian + three rings	$10.033^{+0.006}_{-0.007}$	$58.8^{+0.7}_{-0.7}$	$11.296^{+0.005}_{-0.005}$ $10.3812^{+0.0004}_{-0.0004}$ $10.0773^{+0.0005}_{-0.0005}$	$183.34^{+0.03}_{-0.03}$ $441.41^{+0.06}_{-0.06}$ $589.5^{+0.3}_{-0.3}$	$2.97^{+0.04}_{-0.03}$ $65.7^{+0.1}_{-0.1}$ $181.7^{+0.1}_{-0.1}$

Note. Column (1): target name. Column (2): parametric model assumed for the `galario` fit. Columns (3) and (4): best-fit parameters for inner disk emission. In the case of AA Tau, σ is undefined because the inner disk was modeled with an unresolved point source. Columns (5)–(7): best-fit parameters for ring emission. The median of the marginalized posterior distribution is shown, along with the associated statistical uncertainties from the 16th and 84th percentiles of the MCMC marginalized distribution.

Table B2
`galario` Best-fit Results for 2D Parametric Models

Source	Model	Ring			Arc				
		$\log_{10}(f)$ (Jy sr^{-1})	r (mas)	σ (mas)	$\log_{10}(f)$ (Jy sr^{-1})	r (mas)	σ (mas)	ϕ (deg)	σ_ϕ (deg)
(1)	(2)	(3)	(4)	(5)	(6)	(7)	(8)	(9)	(10)
CQ Tau	Two rings + two arcs	$10.334^{+0.002}_{-0.002}$	$366.0^{+0.2}_{-0.2}$	$41.8^{+0.2}_{-0.2}$	$10.722^{+0.001}_{-0.001}$	$252.2^{+0.2}_{-0.2}$	$62.8^{+0.2}_{-0.2}$	$0.002^{+0.003}_{-0.001}$	$90.2^{+0.3}_{-0.2}$
		$9.856^{+0.005}_{-0.005}$	387^{+2}_{-2}	$133.2^{+0.6}_{-0.6}$	$10.7518^{+0.0007}_{-0.0007}$	$247.1^{+0.1}_{-0.1}$	$58.6^{+0.1}_{-0.2}$	$165.86^{+0.04}_{-0.04}$	$39.21^{+0.07}_{-0.07}$
HD 135344B	One ring + one arc	$10.4123^{+0.0003}_{-0.0003}$	$371.44^{+0.04}_{-0.04}$	$64.98^{+0.06}_{-0.06}$	$10.5283^{+0.0003}_{-0.0003}$	$588.90^{+0.06}_{-0.06}$	$69.48^{+0.05}_{-0.05}$	$146.42^{+0.09}_{-0.07}$	$61.51^{+0.03}_{-0.03}$
HD 143006	Central Gaussian	$10.451^{+0.004}_{-0.003}$	Fixed at 0	$51.3^{+0.3}_{-0.3}$	$10.219^{+0.003}_{-0.003}$	$445.3^{+0.5}_{-0.4}$	$43.8^{+0.3}_{-0.3}$	$129.6^{+0.4}_{-0.3}$	$20.65^{+0.08}_{-0.07}$
	+ two rings + one arc	$10.057^{+0.002}_{-0.002}$	$237.8^{+0.3}_{-0.3}$	$35.7^{+0.4}_{-0.3}$					
		$10.0374^{+0.0008}_{-0.0007}$	$382.7^{+0.4}_{-0.4}$	$64.6^{+0.3}_{-0.3}$					
HD 34282	Three rings + one arc	$9.907^{+0.005}_{-0.004}$	$362.1^{+0.4}_{-0.3}$	$32.2^{+0.7}_{-0.7}$	$10.288^{+0.002}_{-0.002}$	$451.2^{+0.4}_{-0.4}$	$50.8^{+0.3}_{-0.2}$	$20.3^{+0.1}_{-0.1}$	$28.2^{+0.1}_{-0.1}$
		$9.375^{+0.007}_{-0.006}$	407^{+4}_{-4}	386^{+2}_{-2}					
		$10.305^{+0.001}_{-0.001}$	$470.2^{+0.5}_{-0.5}$	$129.0^{+0.3}_{-0.4}$					
MWC 758	Two rings + two arcs	$10.902^{+0.006}_{-0.005}$	$328.7^{+0.1}_{-0.1}$	$2.30^{+0.04}_{-0.05}$	$11.79^{+0.01}_{-0.01}$	$277.37^{+0.04}_{-0.05}$	$1.24^{+0.05}_{-0.04}$	$122.7^{+0.2}_{-0.2}$	$39.2^{+0.2}_{-0.2}$
		$9.8855^{+0.0007}_{-0.0007}$	$432.5^{+0.4}_{-0.4}$	$99.4^{+0.2}_{-0.2}$	$10.551^{+0.001}_{-0.001}$	$550.7^{+0.3}_{-0.3}$	$45.4^{+0.2}_{-0.2}$	$256.1^{+0.1}_{-0.1}$	$20.07^{+0.02}_{-0.02}$

Note. Column (1): target name. Column (2): parametric model assumed for the `galario` fit. Columns (3)–(5): best-fit parameters for ring emission. Columns (6)–(10): best-fit parameters for arc emission. The median of the marginalized posterior distribution is shown, along with the associated statistical uncertainties from the 16th and 84th percentiles of the MCMC marginalized distribution.

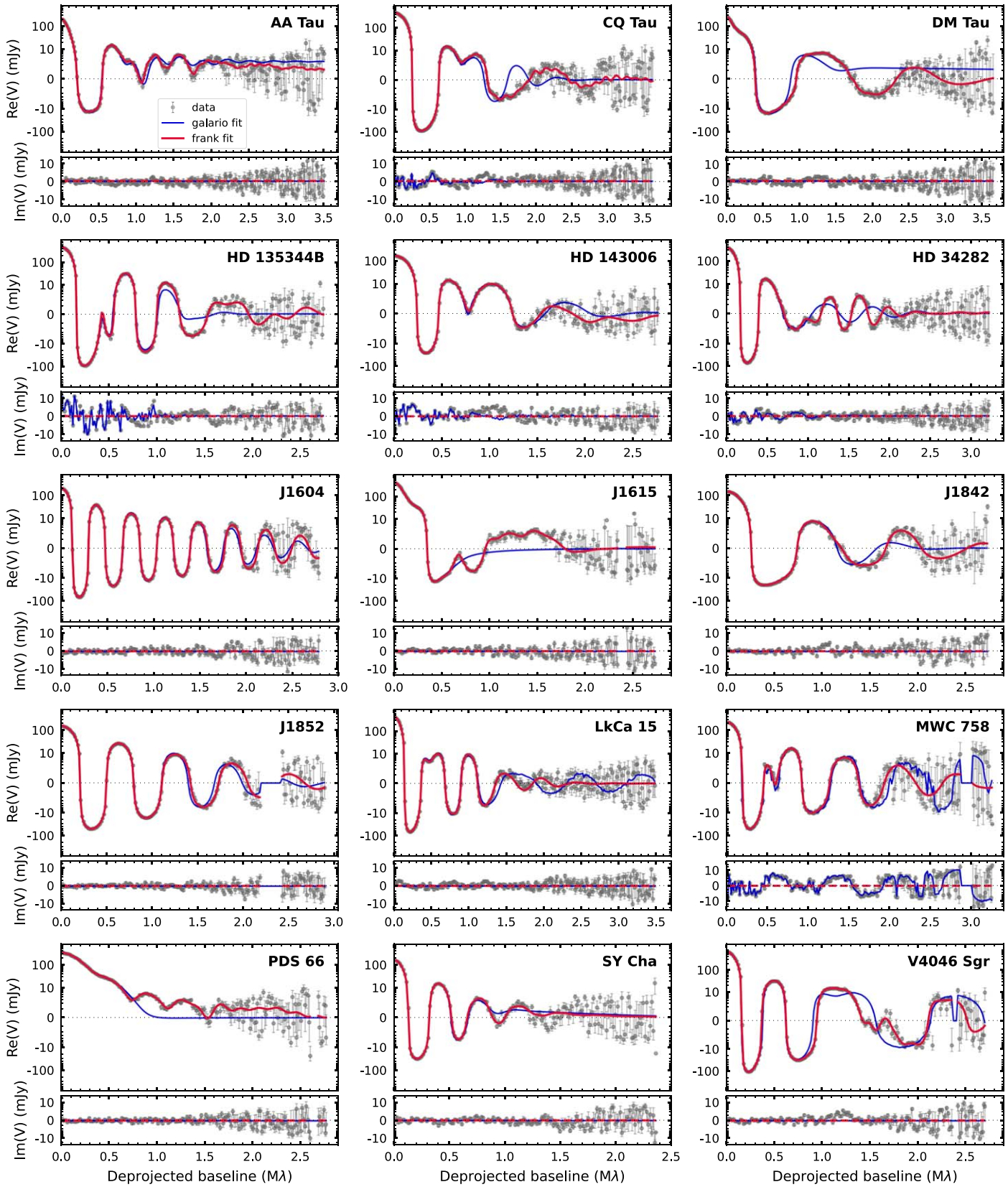

Figure B1. Real and imaginary parts of the recentered and deprojected visibilities azimuthally averaged into 15 kλ wide bins on an asinh scale as a function of the deprojected baseline length for the data (gray points) and the best-fit models from `galario` (blue line) and `frank` (red line). Note that the imaginary part is fitted only when employing a 2D nonaxisymmetric `galario` model (i.e., for CQ Tau, HD 135344B, HD 143006, HD 34282, and MWC 758), while the imaginary components of the `frank` and 1D `galario` axisymmetric models are null for all spatial frequencies by definition.

Appendix C
Comparing Geometrical Parameters Obtained from Continuum and Gas

In Figures C1 and C2 are shown the comparisons between the geometrical parameters (i, PA, ΔR.A., and Δdecl.) derived by analyzing the continuum data with `galario` and the ^{12}CO channel maps with `discminer` (A. F. Izquierdo et al. 2025). We note that most inclination values are within 5°, with the only exception being MWC 758 with about 12°. PAs are all within 10° for disks with relevant inclinations (>25°), whereas the two methods do not agree for low-inclination disks (<25°). Most of the differences in R.A. and decl. offsets are within 50 mas (half of the synthesized beam), with only three cases between 50 and 110 mas.

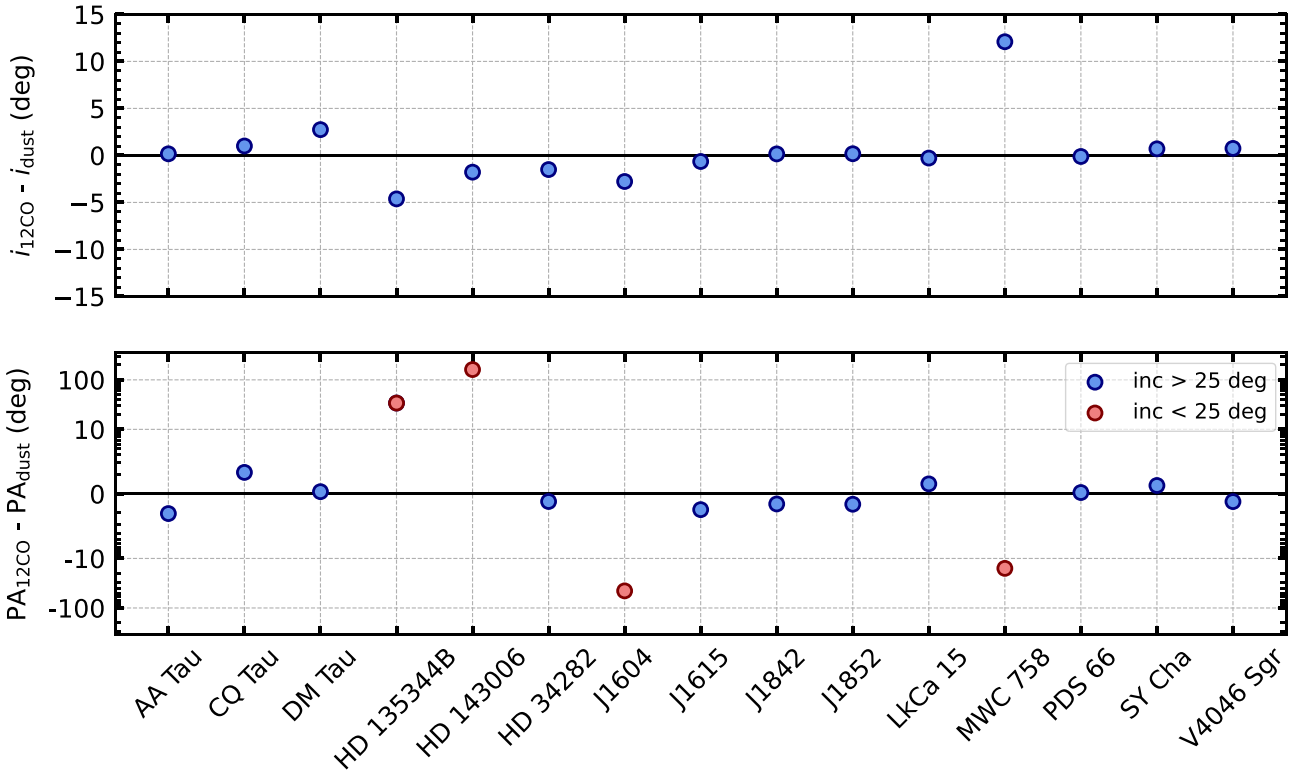

Figure C1. Difference between the i and PA values obtained by analyzing the continuum with `galario` and the ^{12}CO data with `discminer` (A. F. Izquierdo et al. 2025). An asinh stretch has been applied to the y-axis of the bottom panel to include the disks with a large difference in PA due to a low inclination (red circles).

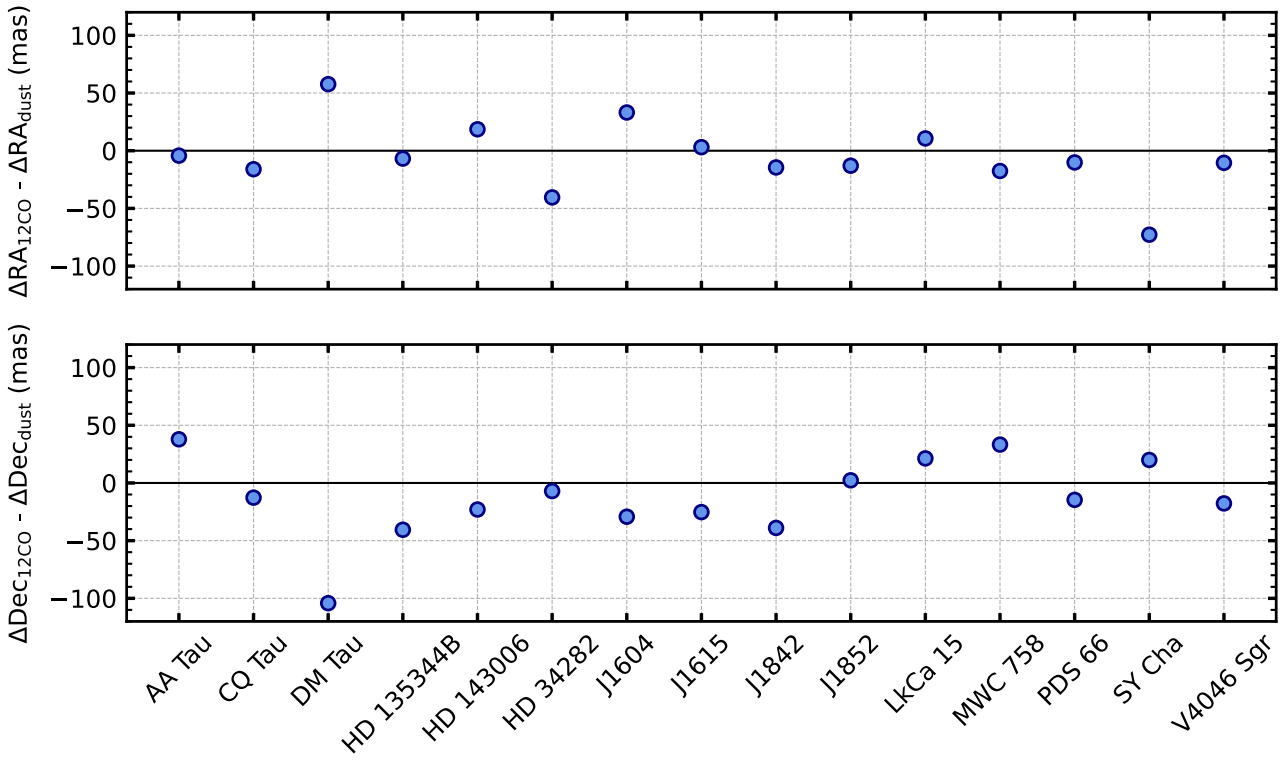

Figure C2. Difference between the offset in R.A. and decl. obtained by analyzing the continuum with `galario` and the ^{12}CO data with `discminer` (A. F. Izquierdo et al. 2025).

Appendix D
Accretion Rate and NIR Excess Values

In Table D1, we report the mass accretion rate $\dot{M}$ and NIR excess for the disks in the exoALMA sample. NIR excess values are obtained as explained in Section 5.2.

Table D1
Accretion Rate and NIR Excess Values of the exoALMA Sample

Source	$\log_{10}\dot{M}$ ($M_\odot$ yr^{-1})	References $\dot{M}$	NIR Excess (%)
(1)	(2)	(3)	(4)
AA Tau	−8.1	J. Bouvier et al. (2013)	4.7 ± 3.6
CQ Tau	−7.0	B. Donehew & S. Brittain (2011)	25.4 ± 2.5
DM Tau	−8.2	C. F. Manara et al. (2014)	<0.6
HD 135344B	−8.0	M. L. Sitko et al. (2012)	27.2 ± 3. 1$^{(a)}$
HD 143006	−8.1	E. Rigliaco et al. (2015)	21.3 ± 1. 4$^{(a)}$
HD 34282	−7.7	J. R. Fairlamb et al. (2015)	9.2 ± 1. 0$^{(a)}$
J1604	−10.5	J. Bouvier et al. (2013)	17.5 ± 3. 6$^{(a)}$
J1615	−8.5	C. F. Manara et al. (2014)	<0. 9$^{(a)}$
J1842	−8.8	C. F. Manara et al. (2014)	12.3 ± 1.1
J1852	−8.7	C. F. Manara et al. (2014)	<1.1
LkCa 15	−8.4	C. F. Manara et al. (2014)	13.4 ± 1.0
MWC 758	−8.0	Y. Boehler et al. (2018)	27.5 ± 2.9
PDS 66	−9.9	L. Ingleby et al. (2013)	7.3 ± 1. 4$^{(a)}$
SY Cha	−9.2	C. F. Manara et al. (2023)	7.6 ± 1. 1$^{(a)}$
V4046 Sgr	−9.3	J. F. Donati et al. (2011)	<0. 9$^{(a)}$

Note. Column (1): target name. Column (2): mass accretion rate. The uncertainty associated with each value is 0.35 dex, following what is reported in Section 2.1.3 of C. F. Manara et al. (2023). Column (3): reference paper for the mass accretion rate values. Column (4): NIR excess. Values with $^{(a)}$ are from A. Garufi et al. (2018), while for disks not included in that work, the NIR excess was calculated following the same procedure (see Appendix D).

Appendix E
Other Correlations with the NAI

Figure E1 shows the correlation between the unscaled accretion rate and the NAI. Figure E2 presents the stellar mass and dust disk mass as functions of the NAI.

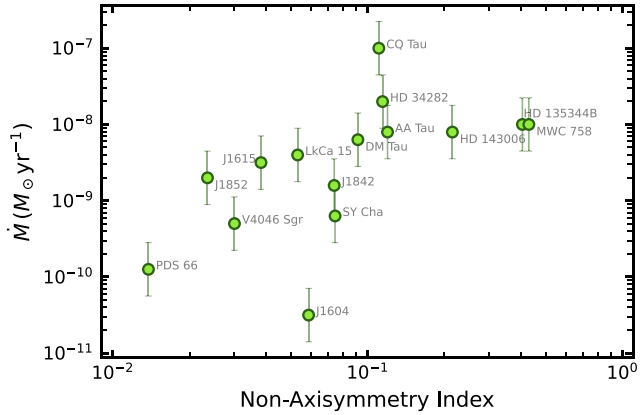

Figure E1. Same as the left panel in Figure 5 but without normalizing the mass accretion rate for its dependence on stellar mass.

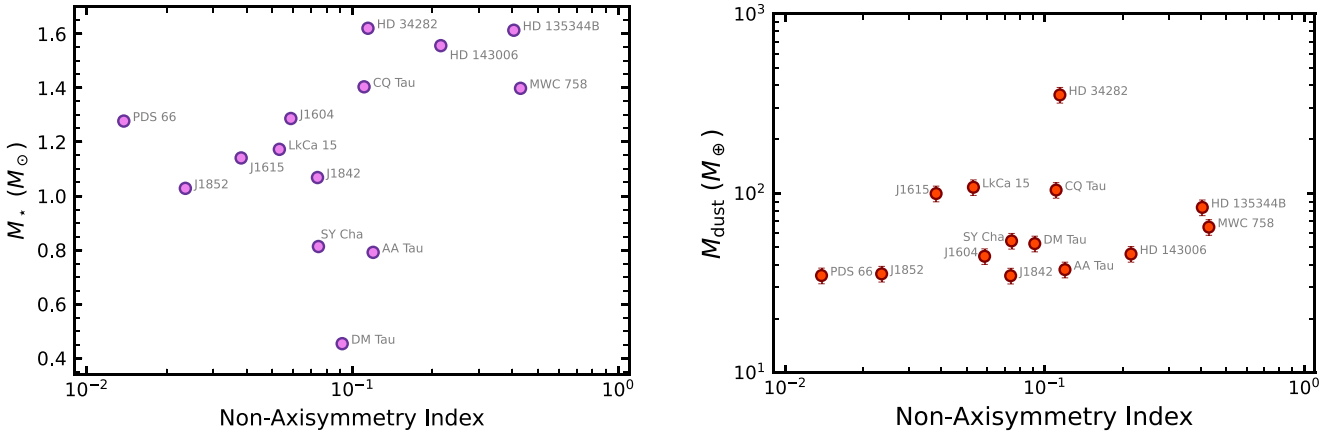

Figure E2. Stellar mass from `discminer` (A. F. Izquierdo et al. 2025) and dust disk mass, calculated in Section 2, as functions of the NAI. The uncertainties in stellar mass are too small to be shown, while for the dust disk mass, we show the 10% absolute flux calibration error, which dominates over the statistical uncertainty.

Appendix F
External Sources in the FOV

To evaluate the presence of external sources in the FOV, we generated a gallery of CLEAN residuals (Figure F1). The CLEAN algorithm was applied using a central mask 3″ wide, a robust parameter of 2.0, and a stopping threshold of 2σ. Notable external sources are apparent within the FOVs of a few targets. For DM Tau, an external source with an integrated flux of approximately 4.0 mJy is located 10.″5 northeast of the central disk. In the FOV of J1842, an external source with an integrated flux of approximately 2.6 mJy is positioned 12.″8 southeast of the central disk, right at the edge of the FOV. Additionally, there is a tentative detection of an external source with an integrated flux of approximately 0.5 mJy within the CQ Tau FOV, 5.″7 north of the central disk. The reported flux density has been computed from the primary-beam-corrected images. We did not find any correspondence of these external sources in the SIMBAD catalog (M. Wenger et al. 2000), the VLA Sky Survey (M. Lacy et al. 2020), or the ALMA continuum source catalogs from the A^{3}COSMOS and A^{3}GOODSS projects (S. Adscheid et al. 2024).

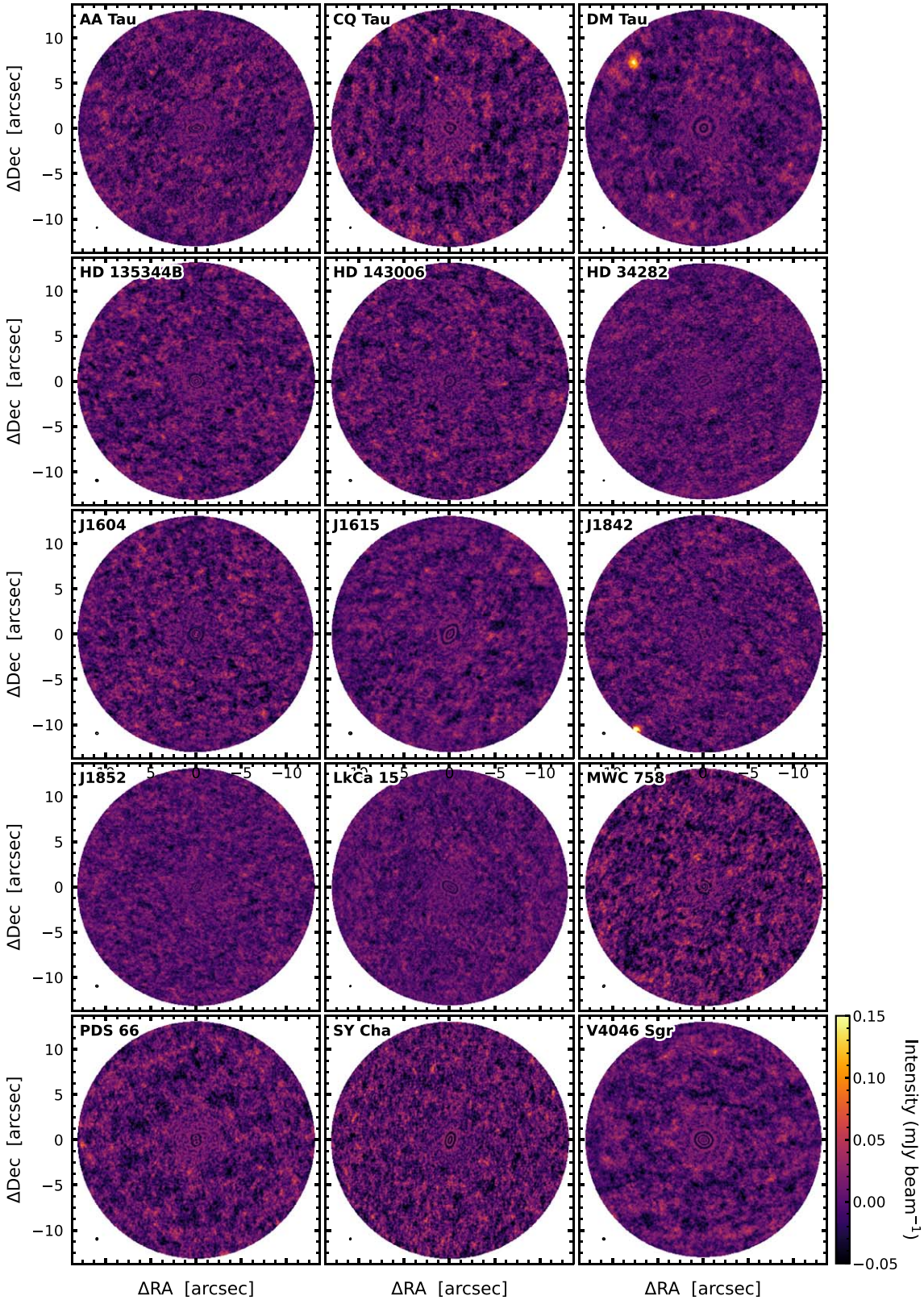

Figure F1. Gallery of CLEAN residuals of the full FOV after deconvolution using a central spherical mask 3″ wide and a 2σ stopping threshold. Each panel shares the same color bar ranging from −0.05 to 0.15 mJy beam^{-1}. The robust value of 2.0 has been employed, and the associated beam is indicated by the black ellipse in the lower left corner of each panel.

ORCID iDs

Pietro Curone https://orcid.org/0000-0003-2045-2154
Stefano Facchini https://orcid.org/0000-0003-4689-2684
Sean M. Andrews https://orcid.org/0000-0003-2253-2270
Leonardo Testi https://orcid.org/0000-0003-1859-3070
Myriam Benisty https://orcid.org/0000-0002-7695-7605
Ian Czekala https://orcid.org/0000-0002-1483-8811
Jane Huang https://orcid.org/0000-0001-6947-6072
John D. Ilee https://orcid.org/0000-0003-1008-1142
Andrea Isella https://orcid.org/0000-0001-8061-2207
Giuseppe Lodato https://orcid.org/0000-0002-2357-7692
Ryan A. Loomis https://orcid.org/0000-0002-8932-1219
Jochen Stadler https://orcid.org/0000-0002-0491-143X
Andrew J. Winter https://orcid.org/0000-0002-7501-9801
Jaehan Bae https://orcid.org/0000-0001-7258-770X
Marcelo Barraza-Alfaro https://orcid.org/0000-0001-6378-7873
Gianni Cataldi https://orcid.org/0000-0002-2700-9676
Nicolás Cuello https://orcid.org/0000-0003-3713-8073
Daniele Fasano https://orcid.org/0000-0003-4679-4072
Mario Flock https://orcid.org/0000-0002-9298-3029
Misato Fukagawa https://orcid.org/0000-0003-1117-9213
Maria Galloway-Sprietsma https://orcid.org/0000-0002-5503-5476
Himanshi Garg https://orcid.org/0000-0002-5910-4598
Cassandra Hall https://orcid.org/0000-0002-8138-0425
Andrés F. Izquierdo https://orcid.org/0000-0001-8446-3026
Kazuhiro Kanagawa https://orcid.org/0000-0001-7235-2417
Geoffroy Lesur https://orcid.org/0000-0002-8896-9435
Cristiano Longarini https://orcid.org/0000-0003-4663-0318
Francois Menard https://orcid.org/0000-0002-1637-7393
Ryuta Orihara https://orcid.org/0000-0003-4039-8933
Christophe Pinte https://orcid.org/0000-0001-5907-5179
Daniel J. Price https://orcid.org/0000-0002-4716-4235
Giovanni Rosotti https://orcid.org/0000-0003-4853-5736
Richard Teague https://orcid.org/0000-0003-1534-5186
Gaylor Wafflard-Fernandez https://orcid.org/0000-0002-3468-9577
David J. Wilner https://orcid.org/0000-0003-1526-7587
Lisa Wölfer https://orcid.org/0000-0002-7212-2416
Hsi-Wei Yen https://orcid.org/0000-0003-1412-893X
Tomohiro C. Yoshida https://orcid.org/0000-0001-8002-8473
Brianna Zawadzki https://orcid.org/0000-0001-9319-1296

References

Adscheid, S., Magnelli, B., Liu, D., et al. 2024, A&A, 685, A1
ALMA Partnership, Brogan, C. L., Pérez, L. M., et al. 2015, ApJL, 808, L3
Aly, H., & Lodato, G. 2020, MNRAS, 492, 3306
Andrews, S. M. 2020, ARA&A, 58, 483
Andrews, S. M., Elder, W., Zhang, S., et al. 2021, ApJ, 916, 51
Andrews, S. M., Huang, J., Pérez, L. M., et al. 2018, ApJL, 869, L41
Andrews, S. M., Wilner, D. J., Zhu, Z., et al. 2016, ApJL, 820, L40
Ansdell, M., Williams, J. P., van der Marel, N., et al. 2016, ApJ, 828, 46
Ayliffe, B. A., Laibe, G., Price, D. J., & Bate, M. R. 2012, MNRAS, 423, 1450
Bae, J., Isella, A., Zhu, Z., et al. 2023, in ASP Conf. Ser. 534, Protostars and Planets VII, ed. S. Inutsuka et al. (San Francisco, CA: ASP), 423
Bae, J., Pinilla, P., & Birnstiel, T. 2018, ApJL, 864, L26
Ballabio, G., Nealon, R., Alexander, R. D., et al. 2021, MNRAS, 504, 888
Beckwith, S. V. W., Sargent, A. I., Chini, R. S., & Guesten, R. 1990, AJ, 99, 924
Benisty, M., Dominik, C., Follette, K., et al. 2023, in ASP Conf. Ser. 534, Protostars and Planets VII, ed. S. Inutsuka et al. (San Francisco, CA: ASP), 605
Benisty, M., Juhasz, A., Boccaletti, A., et al. 2015, A&A, 578, L6
Benisty, M., Juhász, A., Facchini, S., et al. 2018, A&A, 619, A171
Boehler, Y., Ricci, L., Weaver, E., et al. 2018, ApJ, 853, 162
Bouvier, J., Grankin, K., Ellerbroek, L. E., Bouy, H., & Barrado, D. 2013, A&A, 557, A77
Calcino, J., Price, D. J., Pinte, C., et al. 2023, MNRAS, 523, 5763
Carvalho, A. S., Perez, L. M., Sierra, A., et al. 2024, ApJ, 971, 129
CASA Team, Bean, B., Bhatnagar, S., et al. 2022, PASP, 134, 114501
Casassus, S., Christiaens, V., Cárcamo, M., et al. 2021, MNRAS, 507, 3789
Casassus, S., van der Plas, G. M., Perez, S., et al. 2013, Natur, 493, 191
Cazzoletti, P., van Dishoeck, E. F., Pinilla, P., et al. 2018, A&A, 619, A161
Cuello, N., Ménard, F., & Price, D. J. 2023, EPJP, 138, 11
Davis, T. A., Gensior, J., Bureau, M., et al. 2022, MNRAS, 512, 1522
Delussu, L., Birnstiel, T., Miotello, A., et al. 2024, A&A, 688, A81
Dipierro, G., Price, D., Laibe, G., et al. 2015, MNRAS, 453, L73
Donati, J. F., Gregory, S. G., Montmerle, T., et al. 2011, MNRAS, 417, 1747
Donehew, B., & Brittain, S. 2011, AJ, 141, 46
Dong, R., Liu, S.-y., Eisner, J., et al. 2018, ApJ, 860, 124
Drażkowska, J., Bitsch, B., Lambrechts, M., et al. 2023, in ASP Conf. Ser. 534, Protostars and Planets VII, ed. S. Inutsuka et al. (San Francisco, CA: ASP), 717
Facchini, S., Benisty, M., Bae, J., et al. 2020, A&A, 639, A121
Fairlamb, J. R., Oudmaijer, R. D., Mendigutía, I., Ilee, J. D., & van den Ancker, M. E. 2015, MNRAS, 453, 976
Fedele, D., Tazzari, M., Booth, R., et al. 2018, A&A, 610, A24
Foreman-Mackey, D., Hogg, D. W., Lang, D., & Goodman, J. 2013, PASP, 125, 306
Francis, L., Marel, N.v. d., Johnstone, D., et al. 2022, AJ, 164, 105
Francis, L., & van der Marel, N. 2020, ApJ, 892, 111
Gaia Collaboration, Vallenari, A., Brown, A. G. A., et al. 2023, A&A, 674, A1
Galloway-Sprietsma, M., Bae, J., Izquierdo, A. F., et al. 2025, ApJL, 984, L10
Gardner, C. H., Isella, A., Li, H., et al. 2025, ApJL, 984, L16
Garufi, A., Benisty, M., Pinilla, P., et al. 2018, A&A, 620, A94
Hammond, I., Christiaens, V., Price, D. J., et al. 2022, MNRAS, 515, 6109
Hashimoto, J., Muto, T., Dong, R., et al. 2021, ApJ, 911, 5
Hashimoto, P. H., Allard, F., Baron, E., et al. 1999, ApJ, 512, 377
Hildebrand, R. H. 1983, QJRAS, 24, 267
Huang, J., Andrews, S. M., Dullemond, C. P., et al. 2018, ApJL, 869, L42
Huang, J., Andrews, S. M., Dullemond, C. P., et al. 2020, ApJ, 891, 48
Ilee, J. D., Walsh, C., Jennings, J., et al. 2022, MNRAS, 515, L23
Ingleby, L., Calvet, N., Herczeg, G., et al. 2013, ApJ, 767, 112
Izquierdo, A. F., Stadler, J., Galloway-Sprietsma, M., et al. 2025, ApJL, 984, L8
Jennings, J., Booth, R. A., Tazzari, M., Clarke, C. J., & Rosotti, G. P. 2022, MNRAS, 509, 2780
Jennings, J., Booth, R. A., Tazzari, M., Rosotti, G. P., & Clarke, C. J. 2020, MNRAS, 495, 3209
Kurtovic, N. T., Pérez, L. M., Benisty, M., et al. 2018, ApJL, 869, L44
Lacy, M., Baum, S. A., Chandler, C. J., et al. 2020, PASP, 132, 035001
Law, C. J., Loomis, R. A., Teague, R., et al. 2021, ApJS, 257, 3
Lesur, G., Flock, M., Ercolano, B., et al. 2023, in ASP Conf. Ser. 534, Protostars and Planets VII, ed. S. Inutsuka et al. (San Francisco, CA: ASP), 465
Lodato, G., Dipierro, G., Ragusa, E., et al. 2019, MNRAS, 486, 453
Long, F., Andrews, S. M., Zhang, S., et al. 2022, ApJL, 937, L1
Long, F., Pinilla, P., Herczeg, G. J., et al. 2018, ApJ, 869, 17
Longarini, C., Lodato, G., Rosotti, G. P., et al. 2025, ApJL, 984, L17
Longarini, C., Lodato, G., Toci, C., & Aly, H. 2021, MNRAS, 503, 4930
Loomis, R., Facchini, S., Benisty, M., et al. 2025, ApJL, 984, L7
Loomis, R. A., Öberg, K. I., Andrews, S. M., & MacGregor, M. A. 2017, ApJ, 840, 23
Manara, C. F., Ansdell, M., Rosotti, G. P., et al. 2023, in ASP Conf. Ser. 534, Protostars and Planets VII, ed. S. Inutsuka et al. (San Francisco, CA: ASP), 539
Manara, C. F., Testi, L., Natta, A., et al. 2014, A&A, 568, A18
Martinez-Brunner, R., Casassus, S., Pérez, S., et al. 2022, MNRAS, 510, 1248
Mayama, S., Akiyama, E., Panić, O., et al. 2018, ApJL, 868, L3
Orihara, R., Momose, M., Muto, T., et al. 2023, PASJ, 75, 424
Pascucci, I., Cabrit, S., Edwards, S., et al. 2023, in ASP Conf. Ser. 534, Protostars and Planets VII, ed. S. Inutsuka et al. (San Francisco, CA: ASP), 567
Pérez, L. M., Benisty, M., Andrews, S. M., et al. 2018, ApJL, 869, L50
Pérez, L. M., Carpenter, J. M., Andrews, S. M., et al. 2016, Sci, 353, 1519

Pérez, L. M., Isella, A., Carpenter, J. M., & Chandler, C. J. 2014, ApJL, 783, L13
Pérez, S., Casassus, S., Baruteau, C., et al. 2019, AJ, 158, 15
Pinte, C., Ilee, J. D., Huang, J., et al. 2025, ApJL, 984, L15
Pinte, C., Price, D. J., Ménard, F., et al. 2020, ApJL, 890, L9
Quast, G. R., Torres, C. A. O., de La Reza, R., da Silva, L., & Mayor, M. 2000, in IAU Symp. 200, Birth and Evolution of Binary Stars, ed. B. Reipurth & H. Zinnecker (Cambridge: Cambridge Univ. Press), 28
Rampinelli, L., Facchini, S., Leemker, M., et al. 2024, A&A, 689, A65
Ribas, Á., Clarke, C. J., & Zagaria, F. 2024, MNRAS, 532, 1752
Ribas, Á., Macías, E., Weber, P., et al. 2023, A&A, 673, A77
Rigliaco, E., Pascucci, I., Duchene, G., et al. 2015, ApJ, 801, 31
Rosenfeld, K. A., Andrews, S. M., Wilner, D. J., & Stempels, H. C. 2012, ApJ, 759, 119
Rosotti, G. P., Tazzari, M., Booth, R. A., et al. 2019, MNRAS, 486, 4829
Rota, A. A., Meijerhof, J. D., van der Marel, N., et al. 2024, A&A, 684, A134
Ruzza, A., Lodato, G., & Rosotti, G. P. 2024, A&A, 685, A65
Sierra, A., Pérez, L. M., Sotomayor, B., et al. 2024, ApJ, 974, 306
Sierra, A., Pinilla, P., Pérez, L., et al. 2025, MNRAS, 538, 2358
Sitko, M. L., Day, A. N., Kimes, R. L., et al. 2012, ApJ, 745, 29
Speedie, J., Booth, R. A., & Dong, R. 2022, ApJ, 930, 40
Speedie, J., Dong, R., Hall, C., et al. 2024, Natur, 633, 58
Stadler, J., Benisty, M., Izquierdo, A., et al. 2023, A&A, 670, L1
Stadler, J., Benisty, M., Winter, A. J., et al. 2025, ApJL, 984, L11
Sturm, J. A., Rosotti, G. P., & Dominik, C. 2020, A&A, 643, A92
Tazzari, M., Beaujean, F., & Testi, L. 2018, MNRAS, 476, 4527
Teague, R. 2019, JOSS, 4, 1632
Teague, R., Benisty, M., Facchini, S., Fukagawa, M., & Pinte, C. 2024, in press
Testi, L., Birnstiel, T., Ricci, L., et al. 2014, in Protostars and Planets VI, ed. H. Beuther et al. (Tucson, AZ: Univ. of Arizona Press), 339
Ubeira Gabellini, M. G., Miotello, A., Facchini, S., et al. 2019, MNRAS, 486, 4638
van der Marel, N., van Dishoeck, E. F., Bruderer, S., Pérez, L., & Isella, A. 2015, A&A, 579, A106
van der Marel, N., van Dishoeck, E. F., Bruderer, S., et al. 2013, Sci, 340, 1199
van der Plas, G., Ménard, F., Canovas, H., et al. 2017, A&A, 607, A55
Villenave, M., Benisty, M., Dent, W. R. F., et al. 2019, A&A, 624, A7
Weber, P., Casassus, S., & Pérez, S. 2022, MNRAS, 510, 1612
Wenger, M., Ochsenbein, F., Egret, D., et al. 2000, A&AS, 143, 9
Wölfer, L., Barraza-Alfaro, M., Teague, R., et al. 2025, ApJL, 984, L22
Yoshida, C. T., Curone, P., Stadler, J., et al. 2025, ApJL, 984, L19
Zormpas, A., Birnstiel, T., Rosotti, G. P., & Andrews, S. M. 2022, A&A, 661, A66